
Learning Material-Aware Hamiltonian Risk Fields for Safe Navigation

Aditya Sai Ellendula¹, Yi Wang², Chandrajit Bajaj^{1,2}

¹ Department of Computer Science, University of Texas at Austin, Austin, TX 78712, USA

² Oden Institute, University of Texas at Austin, Austin, TX 78712, USA
 {adityase,panzer.wy}@utexas.edu, bajaj@cs.utexas.edu

Abstract

Risk-aware navigation should be selective: a policy should expose evasive degrees of freedom only when the local scene admits a lower-risk feasible maneuver, and suppress them when no safer alternative exists. We show that adding one context-energy term to a port-Hamiltonian navigation policy produces a learned force channel with exactly this falsifiable signature. When the local risk field contains a feasible lower-risk direction, the induced context force activates toward it; when the apparent escape is blocked or not yet available, a route-aware gate suppresses lateral force rather than hallucinating an unsafe maneuver. A CVaR tail-risk objective focuses gradient updates on rare but consequential risk transitions. We validate the selectivity signature across four settings. In the primary delayed-required-escape benchmark, route-aware CVaR reduces premature force activation from 0.950 to 0.180 versus DWA while raising success from 0.480 to 0.810 with zero replans. On real off-road terrain (RELLIS-3D), route-aware enrichment achieves correct activation rate 0.837 and false activation rate 0.114, compared to 0.378/0.752 for scalar risk gradients. On static semantic maps (DFC2018), enrichment reduces catastrophic failure from 0.60 to 0.10 and oscillation by 90.7% while preserving path efficiency. In highway traffic, collisions drop from 100% to 0% when a lane escape is feasible; when no escape exists, the policy suppresses the lateral maneuver. The selectivity property follows from the gradient structure of the context energy rather than from training-time tuning.

1 Introduction

Risk-aware navigation has a selectivity gap. When a lower-risk feasible maneuver exists, the robot should expose the evasive degree of freedom and take it; when the apparent escape is blocked, corrupted, or not yet open, it should suppress that same degree of freedom rather than hallucinate a detour. Classical planners [Hart et al., 1968, Karaman and Frazzoli, 2011], MPC/MPPI-style samplers [Williams et al., 2017], reactive controllers, and learned policies [Schulman et al., 2017, Haarnoja et al., 2018] all address parts of this problem, but none make this activation/suppression asymmetry an explicit structural property: risk costs tend either to pull everywhere a gradient exists, causing false maneuvers, or to be damped enough that the system misses real escape opportunities.

The issue is acute in off-road terrain and local traffic. A patch that looks clear from geometry alone may be wet clay; a corridor that looks low-risk in the semantic map may be physically blocked; a lane change may be useful behind a slow leader but unsafe when the adjacent lane is boxed in. The decision problem is therefore not just to reweight a scalar cost. The agent must decide which force channels should be active under the current local context, and which should remain latent.

Our key observation is that a single additive Hamiltonian energy term can make this selectivity structural. Adding \mathcal{H}_{ctx} to a geometry-only port-Hamiltonian policy simultaneously creates (i) a

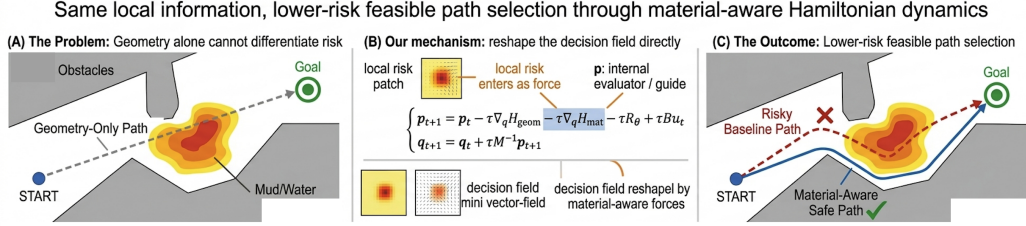


Figure 1: **Selective reshaping of the decision field.** (A) Geometrically feasible maneuvers can differ in material risk. (B) Adding $-\tau \nabla_q \mathcal{H}_{\text{ctx}}$ to the cotangent update creates a context-force channel. (C) The channel bends toward a safer lane when one is feasible, but remains negligible when escape is boxed in. Sec. 4 measures this activation/suppression signature directly.

context force channel in the momentum update, (ii) a parameter subspace and sensitivity stream for learning when that channel matters, and (iii) a route by which CVaR gradients from rare failures act directly on the closed-loop field. Proposition 1 formalizes this coupling: enrichment is not merely a new cost term, but a coordinated enlargement of the force field, learning pathway, and update timescale.

The resulting policy remains a zero-replan local field. New sensory information changes the cotangent update, not an external planner or critic. A local affordance gate tests only the currently sensed patch: when a feasible lower-risk primitive exists, the soft-risk force bends the field toward it; when the candidate is blocked or insufficiently better, the soft channel is suppressed and the rollout stays near the geometry-only policy.

Prior Hamiltonian and port-Hamiltonian learners [Greydanus et al., 2019, Desai et al., 2021, Ellendula et al., 2026] provide structured vector fields, but their geometry-only policy is blind to material/context risk. We extend that policy with soft-risk and hard-hazard force channels and train with CVaR to emphasize rare consequential transitions [Chow et al., 2015]. The primary head-to-head benchmark is a delayed local escape: the lateral maneuver is blocked early, necessary later, and must be timed without global replanning.

Our contributions are:

- **Selective risk-field enrichment.** One additive context-energy term creates a force channel that activates when the local scene admits a lower-risk feasible maneuver and suppresses when it does not. This turns risk adaptation into a context-conditioned change in the closed-loop field, rather than a uniform reweighting of a scalar cost.
- **A learnable energy enrichment principle.** We prove (Proposition 1) that, within the class of port-Hamiltonian learners considered here, a new additive energy term induces a new force channel, parameter subspace, sensitivity stream, and update timescale. The context-enriched enlargement is structurally consistent rather than ad hoc.
- **Falsifiable evaluation across four settings.** We lead with a delayed-required-escape benchmark where the method reduces premature activation while increasing success with zero replans, then measure spatial selectivity (CAR/FAR/SR), temporal selectivity (false pre-activation, suppress rate, reaction delay), and empirical tail-risk reduction (violation CVaR) across RELLIS-3D, RELLIS-Dyn, DFC2018, and highway-env.

The central message of the paper is not that the learner becomes risk-aware. It is that the learner becomes risk-aware *selectively*: reshaping the decision field exactly when the geometry of the situation permits a safer alternative, exposing only the useful degrees of freedom, and leaving the geometry-only behavior unchanged otherwise.

2 Related Work

Structured dynamics and Hamiltonian learning. Hamiltonian and port-Hamiltonian learning provide the closest mechanistic precedent for our view of policy as a structured phase-space flow. Hamiltonian neural networks learn a scalar energy whose symplectic gradient defines the vector

field [Greydanus et al., 2019]; SymODEN extends this idea to controlled systems [Zhong et al., 2020]; Lagrangian networks and port-Hamiltonian neural networks add coordinate or dissipation structure for physical system identification and control [Cranmer et al., 2020, Desai et al., 2021]. Classical port-Hamiltonian theory and energy-shaping control likewise show how damping, interconnection, and external ports can be used to shape closed-loop behavior [van der Schaft and Jeltsema, 2014]. These works motivate our parameterization, but their usual target is dynamics identification or stabilizing control from full-state data. In contrast, we use the Hamiltonian structure as a navigation policy class and add material-risk terms that act directly as learned force channels under local sensing.

Safe and risk-sensitive reinforcement learning. Safe RL typically introduces risk as an objective- or constraint-level quantity. CVaR optimization provides the variational foundation for tail-risk objectives [Rockafellar and Uryasev, 2000]; CVaR MDPs and risk-constrained actor-critic methods optimize tail or percentile risk over trajectories [Chow et al., 2015, 2018]; and constrained policy optimization enforces CMDP-style cost constraints during policy search [Achiam et al., 2017]. Distributional RL instead models the return distribution and can apply risk distortions to that distribution [Bellemare et al., 2017, Dabney et al., 2018]. Our objective uses the same tail-risk lineage, but the object being updated is different: the CVaR signal trains coefficients of a structured decision field, so risk changes the generated forces rather than only a generic policy parameter vector, Lagrange multiplier, or return statistic.

Navigation, local planning, and safety filters. Classical navigation methods adapt paths or local actions through search, sampling, or hand-designed potentials. A* and sampling-based planners provide strong geometric references when map access is available [Hart et al., 1968, Karaman and Frazzoli, 2011]; artificial potential fields, the Dynamic Window Approach, MPPI, and CBF-QP filters produce reactive local behavior under limited information [Khatib, 1985, Fox et al., 1997, Williams et al., 2017, Ames et al., 2017]. These systems are important baselines because they also operate through local costs or forces, but their risk terms are usually hand-designed, externally scored, or enforced as filters. Our method keeps the local closed-loop character while learning how semantic/material risk enters the phase-space update.

Material-aware perception and traversability. Terrain and traversability methods often learn semantic classes, freespace, or cost maps that are then consumed by a planner or controller. Off-road datasets such as RUGD and RELIS-3D support this line of work [Wigness et al., 2019, Jiang et al., 2020], and systems such as TerraPN learn terrain costs for downstream local planning [Sathyamoorthy et al., 2022]. The DFC2018 Houston data provide a complementary remote-sensing setting with rich land-cover cues [IEEE Geoscience and Remote Sensing Society, 2018]. Our DFC experiments use these material labels to construct risk fields, but the contribution is not a new semantic mapper: it is a mechanism for turning material risk into internal energy and force terms that reshape the decision field.

Continual and multi-timescale adaptation. A final related thread studies adaptation over multiple timescales: actor-critic methods separate critic and actor updates, continual learning protects or reuses knowledge across tasks, and rapid motor adaptation conditions policies on recent history [Kirkpatrick et al., 2017, Rusu et al., 2016, Kumar et al., 2021]. Our three loops have a similar motivation—fast local correction, episodic tail-risk updates, and slower curriculum advancement—but the state being adapted is explicitly structured: local corrections and episodic gradients modify Hamiltonian coefficients and material force channels rather than an unconstrained black-box policy.

Prior work therefore covers each ingredient in isolation: structured energy-based dynamics, risk-sensitive objectives, local planners and safety filters, traversability maps, and multi-timescale adaptation. Our contribution is their combination at the point where risk enters the closed loop: a material-energy enrichment that reshapes the Hamiltonian decision field itself.

3 Method

We use two model names to avoid temporal-stage ambiguity. The *geometry-only policy* is the port-Hamiltonian navigator trained without context risk; the *context-enriched field* is the same update after adding one context-energy term and, when used, the local affordance gate. Thus the enrichment is an architectural and training extension, not the second temporal stage of an online rollout. The

added term introduces a learned force channel whose gradient reshapes the closed-loop decision field only when the local scene admits a lower-risk feasible maneuver. At each step the agent observes goal displacement $c_g - c_t$, obstacle features within radius \hat{d} , and a $P \times P$ local context patch P_t containing a smoothed soft-risk field $\tilde{r}(\cdot) \in [0, 1]$ and a signed-distance field $\phi(\cdot)$ to hard hazards. These fields are bilinearly resampled at the current position during integration. All baselines and ablations use the same local-information contract.

3.1 Shared Hamiltonian update

The geometry-only policy and the context-enriched field share the same phase-space update; the only dynamical addition is the boldfaced context-force term in the momentum equation:

Geometry-only policy	Ctx-enriched
$p_{t+1} = p_t - \tau \nabla_q \mathcal{H}_{\text{geom}} - \tau R_\theta(p_t)$	$p_{t+1} = p_t - \tau \nabla_q \mathcal{H}_{\text{geom}} - \tau \nabla_q \mathcal{H}_{\text{ctx}} - \tau R_\theta(p_t)$
$q_{t+1} = q_t + \tau M^{-1} p_{t+1}$ (identical in both fields).	

New sensory information therefore enters through the cotangent variable p , not through a separate critic or global replanner. The decision field is the policy: changing the stored energy changes the vector field that generates the next motion.

3.2 Context energy and route-aware force channel

The context term is additive, so the context-enriched field preserves the geometry-only policy when its context coefficients vanish:

$$\mathcal{H}_\theta(q, p) = \underbrace{\frac{1}{2} p^\top M^{-1} p + \beta D_{\mathcal{G}}(q, \mathbf{c}_g) + \sum_j \alpha_j b_{\text{IPC}}(d_j)}_{\mathcal{H}_{\text{kin}} + \mathcal{H}_{\text{geom}} \text{ (geometry-only)}} + \underbrace{\lambda_s \tilde{r}(\mathbf{c}) + \lambda_h b_{\text{sp}}(\phi(\mathbf{c}))}_{\mathcal{H}_{\text{ctx}} \text{ (Ctx-enriched only)}}. \quad (2)$$

Here b_{IPC} [Li et al., 2020] is the incremental-potential contact barrier and $b_{\text{sp}}(\phi) = k^{-1} \log(1 + e^{k(\hat{d}_\phi - \phi)})$ is a softplus-relaxed inverse SDF. Differentiating \mathcal{H}_{ctx} yields two force channels:

$$F_{\text{ctx}}(\mathbf{c}) = \underbrace{-\lambda_s \nabla \tilde{r}(\mathbf{c})}_{F_{\text{soft}}: \text{ lateral risk deflection}} + \underbrace{-\lambda_h b'_{\text{sp}}(\phi(\mathbf{c})) \nabla \phi(\mathbf{c})}_{F_{\text{hard}}: \text{ hazard repulsion}}, \quad b'_{\text{sp}}(\phi) = -\sigma(k(\hat{d}_\phi - \phi)). \quad (3)$$

F_{soft} expresses preferences among feasible maneuvers, while F_{hard} is a differentiable penalty against boundary contact. It is not a control-barrier certificate; throughout the paper, violation metrics should be read as empirical tail-risk reduction under finite rollouts. Risk is therefore not a post-hoc cost, but a force that reshapes the local closed-loop dynamics.

The scalar soft-risk force can overreact when a low-risk-looking region is blocked by a fence, berm, vehicle, or other non-traversable boundary. We therefore gate only the soft-risk channel using a local affordance test:

$$F_{\text{ctx}}^{\text{ra}}(\mathbf{c}; P_t) = m_{\text{feas}}(\mathbf{c}, z_t) (-\lambda_s \nabla \tilde{r}(\mathbf{c})) - \lambda_h b'_{\text{sp}}(\phi(\mathbf{c})) \nabla \phi(\mathbf{c}), \quad (4)$$

where z_t denotes the finite set of K short-horizon primitives sampled inside the current BEV patch. Let k^* be the feasible primitive with lowest soft-risk exposure, and let k_{geo} be the primitive closest to the geometry-only policy direction. The gate is

$$m_{\text{feas}}(\mathbf{c}, z_t) = \sigma(\kappa_R[(R_{k_{\text{geo}}} - R_{k^*}) - \rho_R]) \sigma(\kappa_C(C_{k^*} - \delta_\phi)) I_{k^*}. \quad (5)$$

Here R_k is the primitive’s soft-risk integral, C_k its minimum SDF clearance, and I_k its local traversability indicator. Thus F_{soft} activates only when the current patch contains a feasible candidate that improves risk by margin ρ_R ; otherwise it is suppressed without weakening F_{hard} . The gate is not a global replanner: it only tests local affordance inside the same sensed patch available to all local-sensing methods. Under semantic or risk-map corruption, the soft channel therefore has a conservative failure mode: a noisy low-risk patch is not enough to activate lateral deflection unless a short-horizon primitive also clears the SDF and improves risk by margin ρ_R . This is not a perception guarantee, but it tends to turn uncertain or inconsistent risk evidence into suppression rather than an unconstrained evasive force. Figure 3 summarizes the gate used in all experiments. Coefficients (λ_s, λ_h) are predicted by sigmoid-bounded CNN heads from P_t fused with the goal token; geometric heads (α, β, γ) are frozen from the geometry-only policy, so these coefficients are the only route by which context alters the field (Appendix A.4).

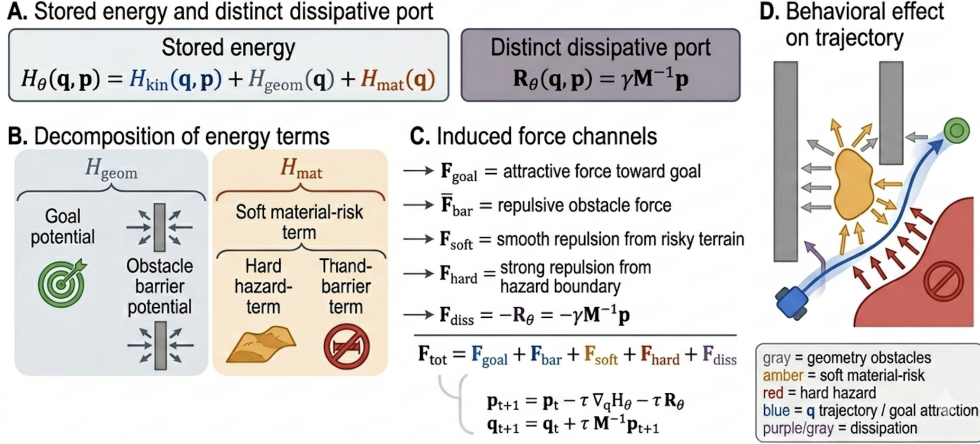


Figure 2: **Factored stored energy and induced force channels.** \mathcal{H}_θ separates kinetic, geometric, dissipative, and context terms. The context term creates a soft-risk deflection channel and a hard-hazard repulsion channel. The route-aware gate lets the soft channel shift the field only when a feasible lower-risk maneuver exists; otherwise the rollout stays near the geometry-only policy.

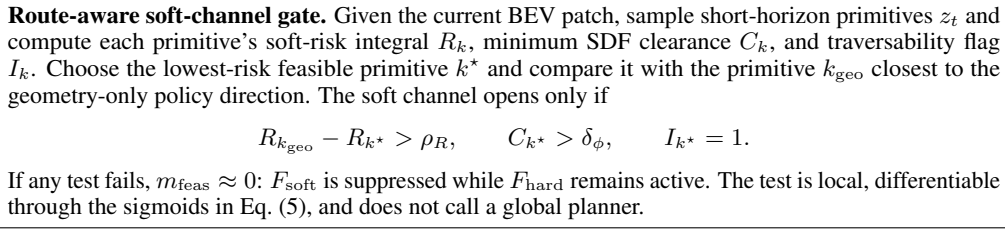


Figure 3: **Gate specification in the main method.** The gate converts a risk-map cue into force activation only when the current local patch contains a cleared, traversable primitive that improves soft risk by margin ρ_R .

3.3 Tail-risk objective

Each rollout accumulates

$$J(\theta) = w_g \|q_T - q_g\|^2 + w_\ell \sum_t \|q_{t+1} - q_t\| + w_r \sum_t \tilde{r}(q_t) \|q_{t+1} - q_t\| + w_h \sum_t \mathbf{1}[\phi(q_t) < \epsilon]. \quad (6)$$

Because the relevant failures are rare, expected-cost training can be dominated by typical rollouts. We therefore optimize the empirical Rockafellar–Uryasev CVaR objective [Rockafellar and Uryasev, 2000]:

$$\widehat{\text{CVaR}}_\alpha(\theta) = \hat{\eta} + \frac{1}{(1-\alpha)B} \sum_{i=1}^B (J^{(i)}(\theta) - \hat{\eta})_+, \quad \hat{\eta} = \widehat{Q}_\alpha(\{J^{(i)}\}_{i=1}^B) \text{ detached}. \quad (7)$$

With $\alpha = 0.95$ and $B = 64$, gradient flows through the worst rollouts, giving a consistent estimator [Hong et al., 2014]. The resulting gradient acts through the sensitivity $\partial q_{t+1} / \partial(\lambda_s, \lambda_h)$ exactly on rollouts where the context force can change the outcome.

3.4 Training hierarchy

The context-enriched field uses three computational roles. First, the geometry-only checkpoint is loaded with $\lambda_s, \lambda_h \equiv 0$, so Eq. (1) initially reproduces the geometry-only policy. Second, the episode loop backpropagates the CVaR loss in Eq. (7) through the differentiable rollout to update the context encoder and coefficient heads. Third, a lightweight segment-correction loop updates active geometry/context coefficients from realized local residuals, while a curriculum loop advances to harder patches only after validation violation rates fall below a threshold. The full loop diagram,

Table 1: **Main-text check of the theory predictions.** We test C1–C3 as finite-rollout predictions, not formal safety certificates. “Below- δ ” means lateral deviation stays below the reaction threshold used for false pre-activation.

Prediction	Rollout condition	Below- δ \uparrow	Failure metric \downarrow
C1	geometry-only delayed escape	1.000	false pre-act 0.000
C2	route-aware context, static blocked R2	0.886	FAR 0.114
C3	route-aware CVaR, pre-escape delayed	0.820	false pre-act 0.180

initialization protocol, and pseudocode are given in Appendix A.7; the main text keeps the algorithmic contract to the force law, loss, and update hierarchy above. For the logged 500-epoch highway runs, the geometry-only policy trained for 1.49 hours and the context-enriched policy for 3.27 hours on one NVIDIA A100 GPU, for 4.8 total GPU-hours.

3.5 Selectivity consequences of context-energy enrichment

The additions above are coupled: adding \mathcal{H}_{ctx} creates the force channel $F_{\text{ctx}} = -\nabla_q \mathcal{H}_{\text{ctx}}$, the coefficient subspace (λ_s, λ_h) , and the rollout-sensitivity pathway through which CVaR training acts. The same structure yields the selectivity consequences measured in Sec. 4.

Proposition 1 (Selectivity consequences of context-energy enrichment). *Let the geometry-only policy and the context-enriched field share the same geometric Hamiltonian, dissipative port R_θ , mass matrix M , and semi-implicit integration rule. Let $\mathcal{H}_{\text{enr}} = \mathcal{H}_{\text{geo}} + \mathcal{H}_{\text{ctx}}$ with $F_{\text{ctx}} = -\nabla_q \mathcal{H}_{\text{ctx}}$. Under the boundedness and local Lipschitz assumptions in Appendix A, the following hold over any finite horizon:*

- C1.** Geometry-only preservation. *If $\sup_t \|F_{\text{ctx}}(q_t)\| \leq \varepsilon$, then the context-enriched rollout remains within $O(\varepsilon)$ of the geometry-only rollout.*
- C2.** No hallucinated escape. *If $\sup_t \|P_\perp F_{\text{ctx}}(q_t)\| \leq \varepsilon_\perp$, then lateral deviation from the geometry-only rollout is bounded by $O(\varepsilon_\perp)$.*
- C3.** Selective risk deflection. *If a feasible lateral direction has projected risk-gradient margin Δ and projected hard-barrier forces cancel the soft-risk force by at most χ , then $\|P_\perp F_{\text{ctx}}\| \geq \lambda_s \Delta - \chi$ and one semi-implicit step decreases local soft risk relative to the geometry-only policy by $O(\tau^2 \lambda_s \Delta^2)$ whenever $\lambda_s \Delta > \chi$.*

Proofs: C1 \Rightarrow Theorem 3; C2 \Rightarrow Corollary 1; C3 \Rightarrow Theorem 4. Selectivity is not trained as a separate label: C1–C3 follow from the gradient structure of \mathcal{H}_{ctx} and the affordance gate, not from post-hoc tuning. Appendix Table 7 makes C1–C3 checkable by mapping each theoretical consequence to measured rollout statistics.

4 Experiments: Selective Hamiltonian Risk Adaptation

The experiments ask one question across four settings: does Hamiltonian context enrichment activate risk forces when a safer feasible alternative exists and suppress them when it does not? We lead with the head-to-head domain where this mechanism is decisive: delayed required escape, where the policy must suppress a tempting lateral maneuver before it is feasible and activate it after the escape opens, all with zero replans.

4.1 Setup, Metrics, and Domains

Research questions. RQ1–RQ2 (spatial): does the context-enriched field activate toward a feasible lower-risk direction and suppress when blocked? RQ3–RQ5 (temporal): does the context-enriched field activate faster than replanning baselines, avoid pursuing closed or unavailable escapes, and suppress-then-activate within one episode? RQ6: must risk enter the force channel, or is loss reweighting sufficient? RQ7: does CVaR training reduce tail violations, not only mean risk?

Table 2: **Delayed-required-escape** benchmark. Escape is blocked before t_{escape} and necessary afterward. The full model best suppresses early false activation while still succeeding after the escape opens. Main rows use 100 paired episodes. [†]Low CVaR with success < 0.21 indicates low exposure from getting stuck; CIs are in Appendix Table 14.

Method	False pre-act \downarrow	Suppress \uparrow	Success \uparrow	Viol. CVaR \downarrow
Geometry-only policy	0.000	1.000	0.030	1.894
Risk-loss-only	0.420	0.580	0.040	1.793
Fixed-coeff context field	0.990	0.010	0.030	0.463 [†]
Black-box CVaR policy	0.920	0.080	0.200	0.503 [†]
DWA semantic	0.950	0.050	0.480	0.695
MPPI semantic	0.950	0.050	0.240	0.831
Ctx-enriched, expected cost	0.370	0.630	0.620	0.855
Route-aware Ctx CVaR	0.180	0.820	0.810	0.740

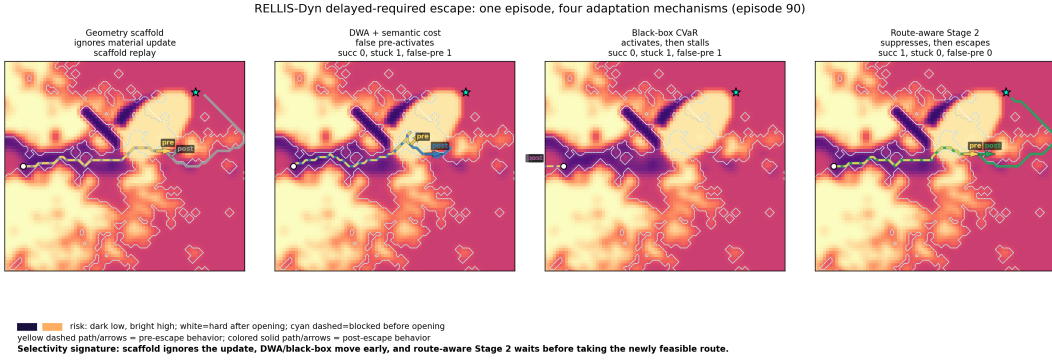


Figure 4: **Qualitative temporal selectivity in one delayed-required escape episode.** Yellow dashed trajectories/arrows show behavior before the escape is available; solid colored trajectories/arrows show behavior after it opens. The geometry-only policy ignores the material update, DWA and black-box CVaR move before the escape is feasible and then stall, while route-aware context enrichment suppresses before t_{escape} and takes the newly feasible route after it opens.

Regimes. All domains share **R1** (feasible lower-risk alternative exists), **R2** (lower-risk-looking direction blocked or dynamically unsafe), and **R3** (risk-neutral; the context-enriched field should preserve geometry-only behavior). RELLIS-Dyn extends R1/R2 from space to time via eight event types spanning soft-risk, hard-boundary, dynamic-obstacle, and compound/delayed scenarios; full definitions are in Appendix B.3. The primary head-to-head benchmark is *delayed required escape*: blocked before t_{escape} , necessary after.

Metrics. Spatial selectivity:

$$\text{CAR} = \Pr[\langle F_{\text{ctx}}, d_{\text{safe}} \rangle > \epsilon \mid R1], \quad \text{FAR} = \Pr[|P_{\perp} F_{\text{ctx}}| > \epsilon \mid R2], \quad \text{SR} = \frac{\mathbb{E}[|P_{\perp} F_{\text{ctx}}| \mid R1]}{\mathbb{E}[|P_{\perp} F_{\text{ctx}}| \mid R2]}, \quad (8)$$

and AUPRC (threshold-independent). Temporal: *reaction delay* (δ -displacement from the pre-event geometry-only trajectory; sensitivity in Appendix Table 17), *stale exposure* (violation before reaction), *false pre-activation* (lateral force before t_{escape}), *suppress rate* ($1 - \text{false pre-activation}$). Post-event *violation CVaR* (hard contact weighted separately) is the primary tail metric.

4.2 Primary Head-to-Head: Delayed Required Escape

All methods receive the same updated BEV patch at every step; only the decision mechanism differs. Table 2 is the main head-to-head result: the route-aware CVaR field reduces DWA and semantic MPPI false pre-activation from 0.950 to 0.180 while raising success from 0.480/0.240 to 0.810, and does so without replans. The table also isolates the three ingredients: Hamiltonian force structure, CVaR timing, and context-conditioned coefficients.

Table 3: **RELLIS-3D spatial selectivity.** Route-aware context enrichment achieves the best SR and AUPRC, indicating selective activation rather than uniform risk-gradient following. Fixed coefficients fail to suppress in blocked scenes (FAR 0.888).

Method	CAR \uparrow	FAR \downarrow	SR \uparrow	AUPRC \uparrow
Geometry-only policy	0.000	0.000	0.000	0.000
Scalar context field	0.378	0.752	1.031	0.008
Fixed-coeff context field	0.566	0.888	1.123	0.008
Non-route directional Ctx	0.135	0.178	1.165	0.206
Black-box CVaR policy	0.884	0.129	1.292	0.206
Route-aware Ctx	0.837	0.114	2.358	0.289

Table 4: **RELLIS-Dyn 3-event material aggregate.** All methods receive the same updated BEV patch. The gate uses only $K=8$ local primitives, not graph search or trajectory optimization. \dagger Oracle has global map access. \ddagger Delay includes gate-suppressed R2 episodes; see Table 2.

Method	Family	Succ. \uparrow	Soft CVaR \downarrow	Delay \downarrow	Stuck \downarrow	Replans \downarrow	ms/step \downarrow
Geometry-only policy	geom.-only	1.000	0.712	16.2	0.04	0	0.8
Risk-loss-only	learned loss	1.000	0.673	13.4	0.03	0	0.9
Fixed-coeff Ctx	learned field	0.120	0.459	1.47	0.74	0	1.4
Black-box CVaR	learned field	0.273	0.482	3.61	0.61	0	4.2
Ctx-enriched, exp.cost	learned field	0.983	0.465	1.30	0.02	0	2.1
DWA semantic	reactive	0.567	0.621	2.8	0.43	0	0.6
CBF-QP	safety filter	0.890	0.651	7.4	0.09	0	0.9
Local A* (budget)	planner	0.983	0.629	4.6	0.01	9.8	8.4
MPC (budget)	planner	0.967	0.624	3.8	0.03	11.1	42.2
Route-aware Ctx	learned field	0.980	0.638	1.8\ddagger	0.06	0	2.3
Oracle replanner	planner \dagger	1.000	0.601	1.9	0.00	68.3	97.5

Hamiltonian structure: black-box CVaR uses the same CVaR objective and BEV patch but no Hamiltonian force channel; false pre-activation 0.920, success 0.200 vs. 0.810. Static CAR 0.884 does not transfer to temporal suppression. *CVaR training:* same architecture, different objective; CVaR halves false pre-activation (0.370 \rightarrow 0.180), raises suppression (0.630 \rightarrow 0.820), improves success by 30%, reduces violation CVaR (0.855 \rightarrow 0.740). *Context-conditioning:* fixed vs. CNN-predicted (λ_s, λ_h); success 0.030 vs. 0.810. Without adaptive coefficients the method suppresses nothing.

4.3 RELLIS-3D: Spatial Selectivity

Table 3 reports six variants on 2,250 BEV episodes (leave-one-sequence-out; CIs in Appendix Table 11). The SR gap between black-box CVaR (1.292) and route-aware context-enriched field (2.358) is the spatial analog of the temporal gap in Table 2: the black-box learns *when* risk gradients exist but not *whether* following them is safe. The route-aware gate produces the selectivity; Section 4.2 shows the same architecture without the gate (black-box) collapses to 0.200 navigation success on the strictest temporal test.

4.4 RELLIS-Dyn: Temporal Selectivity

Material-event aggregate. Table 4 reports the three-event material subset (mud onset, corridor closes, corridor opens) at 100 episodes per event. Black-box CVaR success 0.273 on the same task where it achieves CAR 0.884 confirms that static selectivity metrics do not predict navigation success. Risk-loss-only hard exposure 0.694 vs. Route-aware Ctx 0.027 supports RQ6: the risk signal must enter the force channel. The route-aware context-enriched field is the strongest zero-replan learned-field method, matching planning baselines that use 9–68 explicit replans. Corridor-opens trajectory detail is in Appendix Figure 8; the eight-event breakdown (including moving-obstacle events where DWA is architecturally stronger) is in Appendix Table 16.

Table 5: **DFC2018 outcome shift** (300 paired episodes).

Method	Succ.↑	Cat.fail↓	Hard len.↓	Risk↓	Len.ratio	Osc.↓
Geometry-only policy	0.867	0.600	21.106	23.267	1.044	82.212
Ctx-enriched	1.000	0.100	0.658	9.493	1.045	7.629

Table 6: **Highway mechanism ablation** (200 paired seeds). The lateral channel enables passing; the TTC channel prevents using it when the adjacent maneuver is unsafe.

Variant	Def.off-rd↓	Slow coll↓	Slow succ↑	Boxed coll↓	Boxed off-rd↓	Boxed spd↑
No lateral context	0.00	1.00	0.00	1.00	0.00	22.33
Lateral only	0.20	0.00	1.00	1.00	0.00	22.33
Lateral + TTC	0.00	0.00	1.00	0.00	0.00	7.57

Within-episode temporal selectivity. Figure 4 shows the delayed-required-escape mechanism qualitatively. Route-aware CVaR suppresses lateral activation throughout the blocked window and activates within two steps of t_{escape} (false pre-activation 0.180). The expected-cost variant activates earlier (0.370), directly demonstrating CVaR’s tail-gradient contribution. DWA false pre-activates on 95% of episodes, typically 3–5 steps before t_{escape} , because partial boundary changes trigger its reactive response before the escape is fully open.

4.5 DFC2018: Geometry-Only Repair

Table 5 shows enrichment repairs a geometry-only policy on a static semantic material map: success $0.867 \rightarrow 1.000$, catastrophic failure $0.600 \rightarrow 0.100$, hard-hazard traversal -96.9% , cumulative risk -59.2% , oscillation -90.7% , path-length ratio unchanged. Full planner comparison in Appendix B.1; full-map planners with global access obtain lower raw risk but the context-enriched field produces smoother trajectories with zero oscillation.

4.6 Highway-env: Interaction Selectivity

The open slow-leader scenario is the interaction analog of corridor opens (lateral channel should activate); the boxed scenario is the analog of moving-obstacle-blocks-detour (channel should suppress). Table 6 shows the mechanism ablation: removing the lateral channel causes collision with the slow leader on every episode; adding it without the TTC channel causes off-road failure in the boxed scenario; only the full system passes and suppresses correctly. MOBIL-IDM and risk-aware MPC outperform the context-enriched field overall (Appendix Table 18); the context-enriched field is the strongest learned method and the only one exhibiting the intended activation/suppression split.

4.7 Interpretation and Limitations

Tradeoff positions. Reactive baselines (DWA, CBF-QP) handle hard-boundary events well but false pre-activate on discovery events (DWA: 0.950 on delayed escape). Planning baselines reduce violation under replan budget but pay $9\text{--}68\times$ more replans. The route-aware context-enriched field occupies the zero-replan gradient-following frontier: strongest on soft-risk and escape-discovery events, weaker on moving-obstacle events where reactive boundary following suffices. The eight-event Pareto (Appendix Figure 9) shows the full tradeoff surface.

Limitations. (i) $b_{\text{sp}}(\phi)$ is a differentiable barrier, not a CBF certificate; our claims are empirical tail-risk reductions, not forward-invariance guarantees (Appendix A, §A.9). (ii) Performance depends on risk-map quality; at 20–30% label corruption, CAR/FAR degrade despite the gate’s tendency to suppress inconsistent soft-risk evidence (Appendix Table 13). (iii) Gate overhead must be profiled on latency-constrained hardware (ms/step in Table 4).

5 Conclusion

One additive context-energy term gives a port-Hamiltonian policy a falsifiable selectivity signature: activate when a safer feasible alternative exists and suppress otherwise. Ablations isolate Hamiltonian structure, CVaR tail timing, and context-conditioned coefficients; the pattern holds across off-road, semantic, dynamic, and highway settings without global replanning.

Social Impact Statement. This work uses public or simulated navigation data and does not rely on private user information. Its intended benefit is more reliable autonomous navigation under terrain and traffic uncertainty. The method is not a deployment safety certificate: real systems would require independent validation, fallback control, and monitoring.

Acknowledgement. This research was supported in part by a grant from the Peter O’Donnell Foundation, the Michael J Fox Foundation, Jim Holland- Backcountry Foundation and in part from a grant from the Army Research Office accomplished under Cooperative Agreement Number W911NF-19-2-0333

References

- Joshua Achiam, David Held, Aviv Tamar, and Pieter Abbeel. Constrained policy optimization. In *Proceedings of the 34th International Conference on Machine Learning (ICML)*, volume 70, pages 22–31, 2017.
- Aaron D. Ames, Xiangru Xu, Jessy W. Grizzle, and Paulo Tabuada. Control barrier function based quadratic programs for safety critical systems. *IEEE Transactions on Automatic Control*, 62(8): 3861–3876, 2017.
- Peter L. Bartlett and Shahar Mendelson. Rademacher and gaussian complexities: Risk bounds and structural results. *Journal of Machine Learning Research*, 3:463–482, 2002.
- Marc G. Bellemare, Will Dabney, and Rémi Munos. A distributional perspective on reinforcement learning. In *Proceedings of the 34th International Conference on Machine Learning*, pages 449–458, 2017.
- Yinlam Chow, Aviv Tamar, Shie Mannor, and Marco Pavone. Risk-sensitive and robust decision-making: A CVaR optimization approach. In *Advances in Neural Information Processing Systems (NeurIPS)*, volume 28, pages 1522–1530, 2015.
- Yinlam Chow, Mohammad Ghavamzadeh, Lucas Janson, and Marco Pavone. Risk-constrained reinforcement learning with percentile risk criteria. *Journal of Machine Learning Research*, 18 (167):1–51, 2018.
- Miles Cranmer, Sam Greydanus, Stephan Hoyer, Peter Battaglia, David Spergel, and Shirley Ho. Lagrangian neural networks. In *ICLR Workshop on Integration of Deep Neural Models and Differential Equations*, 2020.
- Will Dabney, Georg Ostrovski, David Silver, and Rémi Munos. Implicit quantile networks for distributional reinforcement learning. In *Proceedings of the 35th International Conference on Machine Learning*, pages 1096–1105, 2018.
- Shaan A. Desai, Marios Mattheakis, David Sondak, Pavlos Protopapas, and Stephen J. Roberts. Port-hamiltonian neural networks for learning explicit time-dependent dynamical systems. *Physical Review E*, 104(3):034312, 2021. doi: 10.1103/PhysRevE.104.034312. URL <https://doi.org/10.1103/PhysRevE.104.034312>.
- Aryeh Dvoretzky, Jack Kiefer, and Jacob Wolfowitz. Asymptotic minimax character of the sample distribution function and of the classical multinomial estimator. *The Annals of Mathematical Statistics*, 27(3):642–669, 1956.
- Aditya Sai Ellendula, Yi Wang, Minh Nguyen, and Chandrajit Bajaj. Grl-snam: Geometric reinforcement learning with path differential hamiltonians for simultaneous navigation and mapping in unknown environments, 2026. URL <https://arxiv.org/abs/2601.00116>.

- Dieter Fox, Wolfram Burgard, and Sebastian Thrun. The dynamic window approach to collision avoidance. *IEEE Robotics & Automation Magazine*, 4(1):23–33, 1997.
- Samuel Greydanus, Misko Dzamba, and Jason Yosinski. Hamiltonian neural networks. In *Advances in Neural Information Processing Systems (NeurIPS)*, volume 32, 2019.
- Tuomas Haarnoja, Aurick Zhou, Pieter Abbeel, and Sergey Levine. Soft actor-critic: Off-policy maximum entropy deep reinforcement learning with a stochastic actor, 2018. URL <https://arxiv.org/abs/1801.01290>.
- Peter E. Hart, Nils J. Nilsson, and Bertram Raphael. A formal basis for the heuristic determination of minimum cost paths. *IEEE Transactions on Systems Science and Cybernetics*, 4(2):100–107, 1968. doi: 10.1109/TSSC.1968.300136. URL <https://doi.org/10.1109/TSSC.1968.300136>.
- L. Jeff Hong, Zhaolin Hu, and Guangwu Liu. Monte carlo estimation of value-at-risk, conditional value-at-risk and their sensitivities. *Proceedings of the 2014 Winter Simulation Conference*, pages 95–107, 2014.
- IEEE Geoscience and Remote Sensing Society. 2018 IEEE GRSS Data Fusion Contest: Multispectral lidar, hyperspectral, and rgb data for urban land-cover classification. <https://www.grss-ieee.org/community/technical-committees/2018-ieee-grss-data-fusion-contest/>, 2018.
- Peng Jiang, Philip Osteen, Maggie Wigness, and Srikanth Saripalli. RELLIS-3D dataset: Data, benchmarks and analysis, 2020. URL <https://arxiv.org/abs/2011.12954>.
- Sertac Karaman and Emilio Frazzoli. Sampling-based algorithms for optimal motion planning. *The International Journal of Robotics Research*, 30(7):846–894, 2011.
- Oussama Khatib. Real-time obstacle avoidance for manipulators and mobile robots. In *IEEE International Conference on Robotics and Automation*, pages 500–505, 1985.
- James Kirkpatrick, Razvan Pascanu, Neil Rabinowitz, Joel Veness, Guillaume Desjardins, Andrei A. Rusu, Kieran Milan, John Quan, Tiago Ramalho, Agnieszka Grabska-Barwinska, et al. Overcoming catastrophic forgetting in neural networks. *Proceedings of the National Academy of Sciences*, 114(13):3521–3526, 2017.
- Ashish Kumar, Zipeng Fu, Deepak Pathak, and Jitendra Malik. RMA: Rapid motor adaptation for legged robots. In *Robotics: Science and Systems (RSS)*, 2021.
- Minchen Li, Zachary Ferguson, Teseo Schneider, Timothy R. Langlois, Denis Zorin, Daniele Panozzo, Chenfanfu Jiang, and Danny M. Kaufman. Incremental potential contact: Intersection- and inversion-free, large-deformation dynamics. *ACM Transactions on Graphics*, 39(4):49, 2020.
- Pascal Massart. The tight constant in the dvoretzky-kiefer-wolfowitz inequality. *The Annals of Probability*, 18(3):1269–1283, 1990.
- Mitio Nagumo. Über die lage der integralkurven gewöhnlicher differentialgleichungen. *Proceedings of the Physico-Mathematical Society of Japan*, 24:551–559, 1942.
- R. Tyrrell Rockafellar and Stanislav Uryasev. Optimization of conditional value-at-risk. *Journal of Risk*, 2(3):21–42, 2000.
- Andrei A. Rusu, Neil C. Rabinowitz, Guillaume Desjardins, Hubert Soyer, James Kirkpatrick, Koray Kavukcuoglu, Razvan Pascanu, and Raia Hadsell. Progressive neural networks, 2016. URL <https://arxiv.org/abs/1606.04671>.
- Adarsh Jagan Sathyamoorthy, Kasun Weerakoon, Tianrui Guan, Jing Liang, and Dinesh Manocha. Terrapn: Unstructured terrain navigation using online self-supervised learning. In *2022 IEEE/RSJ International Conference on Intelligent Robots and Systems (IROS)*, pages 7197–7204. IEEE, 2022.
- John Schulman, Filip Wolski, Prafulla Dhariwal, Alec Radford, and Oleg Klimov. Proximal policy optimization algorithms, 2017. URL <https://arxiv.org/abs/1707.06347>.

- Shai Shalev-Shwartz and Shai Ben-David. *Understanding Machine Learning: From Theory to Algorithms*. Cambridge University Press, 2014.
- Alexander Shapiro, Darinka Dentcheva, and Andrzej Ruszczyński. *Lectures on Stochastic Programming: Modeling and Theory*. SIAM, 2009.
- Arjan van der Schaft and Dimitri Jeltsema. Port-hamiltonian systems theory: An introductory overview. *Foundations and Trends in Systems and Control*, 1(2–3):173–378, 2014.
- Maggie Wigness, Sungmin Eum, John G. Rogers, David Han, and Heesung Kwon. A RUGD dataset for autonomous navigation and visual perception in unstructured outdoor environments. In *IEEE/RSJ International Conference on Intelligent Robots and Systems (IROS)*, pages 5000–5007, 2019. doi: 10.1109/IROS40897.2019.8968283. URL <https://doi.org/10.1109/IROS40897.2019.8968283>.
- Grady Williams, Nolan Wagener, Brian Goldfain, Paul Drews, James M. Rehg, Byron Boots, and Evangelos A. Theodorou. Information theoretic mpc for model-based reinforcement learning. In *IEEE International Conference on Robotics and Automation (ICRA)*, pages 1714–1721, 2017.
- Yaofeng Desmond Zhong, Biswadip Dey, and Amit Chakraborty. Symplectic ODE-Net: Learning Hamiltonian dynamics with control. In *International Conference on Learning Representations (ICLR)*, 2020.

A Theoretical Guarantees for Contextual Hamiltonian Enrichment

This appendix collects the formal properties used in Section 3.6. The goal is not to claim unconditional safety or global optimality. Instead, we prove that contextual Hamiltonian enrichment has five conditional properties aligned with the central claims of the paper: (i) an added energy term induces a new force and sensitivity channel; (ii) the enriched system preserves the port-Hamiltonian dissipativity structure; (iii) the discrete rollout is practically dissipative for small enough step size; (iv) when context gradients vanish, the context-enriched field remains close to the geometry-only policy and cannot generate a spurious lateral escape; and (v) when a projected risk-gradient margin exists, the contextual force activates and locally reduces risk. We also justify the detached-quantile CVaR gradient used in the episode loop and state the constrained risk-averse OCP interpretation used by the upper-confidence update. The passivity arguments follow the standard port-Hamiltonian energy balance [van der Schaft and Jeltsema, 2014, Desai et al., 2021]; the CVaR argument uses the Rockafellar–Uryasev variational representation [Rockafellar and Uryasev, 2000] and standard empirical quantile sensitivity arguments [Hong et al., 2014].

A.1 Setup and notation

Let $q \in \mathbb{R}^d$ denote the configuration coordinate and $p \in \mathbb{R}^d$ its cotangent variable. Let $x = (q, p)$, let $M \succ 0$ be the mass matrix, and write

$$v = M^{-1}p.$$

The geometry-only Hamiltonian is

$$H_{\text{scaf}}(q, p) = \frac{1}{2}p^\top M^{-1}p + H_{\text{geom}}(q),$$

where H_{geom} contains the goal and geometric barrier terms. The context-enriched field adds the context Hamiltonian

$$H_{\text{ctx}}(q; z) = \lambda_s \tilde{r}(\mathbf{c}; z) + \lambda_h b_{\text{sp}}(\phi(\mathbf{c}; z)),$$

where \mathbf{c} is the workspace position component of q , z denotes the locally sensed context patch, \tilde{r} is the smoothed soft-risk field, and ϕ is the signed-distance field for hard hazards. Thus

$$H_{\text{enr}}(q, p; z) = H_{\text{scaf}}(q, p) + H_{\text{ctx}}(q; z).$$

The corresponding context force is

$$F_{\text{ctx}}(q; z) = -\nabla_q H_{\text{ctx}}(q; z) = -\lambda_s \nabla_q \tilde{r}(\mathbf{c}; z) - \lambda_h b'_{\text{sp}}(\phi(\mathbf{c}; z)) \nabla_q \phi(\mathbf{c}; z).$$

This is exactly the soft-risk plus hard-hazard force decomposition used in the main paper.

The continuous-time enriched port-Hamiltonian dynamics are

$$\dot{q} = \nabla_p H_{\text{enr}}(q, p; z) = M^{-1}p, \quad (9)$$

$$\dot{p} = -\nabla_q H_{\text{enr}}(q, p; z) - D(q, p; z)M^{-1}p + B(q, p; z)u, \quad (10)$$

where $D(q, p; z) \succeq 0$ is the dissipative port. The rollout used in the paper is the semi-implicit update

$$p_{t+1} = p_t - \tau \nabla_q H_{\text{geom}}(q_t) - \tau \nabla_q H_{\text{ctx}}(q_t; z_t) - \tau D_t M^{-1}p_t + \tau B_t u_t, \quad (11)$$

$$q_{t+1} = q_t + \tau M^{-1}p_{t+1}. \quad (12)$$

When $D_t M^{-1}p_t$ is implemented as the scalar dissipative port $R_\theta(q_t, p_t) = \gamma M^{-1}p_t$, this reduces to the update in the main text.

Assumption 1 (Rollout regularity). There exists a compact rollout tube $\mathcal{K} \subset \mathbb{R}^{2d}$ such that the geometry-only and context-enriched trajectories remain in \mathcal{K} for the horizon under analysis. On \mathcal{K} , H_{geom} and H_{ctx} are C^2 , and their gradients are Lipschitz.

Assumption 2 (Bounded context force). There exists $G_{\text{ctx}} < \infty$ such that

$$\|\nabla_q H_{\text{ctx}}(q; z)\| \leq G_{\text{ctx}}$$

for all $(q, p) \in \mathcal{K}$ and all context patches considered.

Assumption 3 (Dissipative port). There exists $\rho \geq 0$ such that

$$D(q, p; z) \succeq \rho I$$

on \mathcal{K} . When $\rho > 0$, the system is strictly dissipative in velocity.

Assumption 4 (Local Lipschitz rollout map). The shared geometry-only update map is locally Lipschitz on \mathcal{K} : there exists $L_\Phi \geq 0$ such that one step of the shared dynamics amplifies state errors by at most $1 + \tau L_\Phi$.

A.2 Full local-risk interface and problem setup

At each time step t the agent observes a goal displacement $\mathbf{c}_g - \mathbf{c}_t$, locally-sensed obstacle or neighbor features $\{(C_j, R_j, W_j)\}_{j=1}^{N(t)}$ within sensing radius \hat{d} , and a $P \times P$ context patch P_t centered at the current position. The patch contains a smoothed risk field $\tilde{r}(\cdot) \in [0, 1]$ and a signed-distance field $\phi(\cdot)$ to hard hazards or infeasible regions. Depending on the domain, \tilde{r} may encode material risk, traffic interaction risk, or a procedurally constructed local interaction field; the method only requires that the field be locally queryable and differentiable after smoothing. The patch is bilinearly resampled at the agent’s current position at every integration step, so forces and costs reflect the actual path traversed. All comparisons use the same local-information regime; differences come from the decision mechanism, not from privileged sensing.

Each observation defines a local optimization instance. The goal term, clearance barriers, context-risk preference, hazard barrier, and lateral-motion channel form a product space of potential actions and penalties, but only some factors are active in a given context. We use *action-space adaptation* in this restricted continuous sense: the learner does not enumerate discrete actions, but changes which force channels have non-negligible magnitude under the sensed context.

Static and dynamic risk. The same interface covers both static and dynamic settings. In DFC and RELLIS, \tilde{r} and ϕ are fixed semantic/material fields, so risk exposure depends on the path taken through the map. In highway-env, the local patch changes as neighboring vehicles move, close gaps, or block lateral escape. Static domains test context-enriched path selection; dynamic domains test whether the learned field preserves clearance, time-to-collision, and maneuvering room before violations become terminal.

A.3 Route-aware gate: full specification

The main text uses the gate $m_{\text{feas}} \in [0, 1]$ in Eq. (4) without specifying its computation. This subsection gives the full specification.

From the current state q_t we roll out K short-horizon motion primitives $\{\xi_k\}_{k=1}^K$ inside the sensed BEV window P_t and compute for each candidate:

$$R_k = \int_{\xi_k} \tilde{r}(s) ds, \quad C_k = \min_{\xi_k} \phi(s), \quad I_k = \mathbf{1}[C_k > \delta_\phi \text{ and } \xi_k \subset \mathcal{T}(P_t)], \quad (13)$$

where $\mathcal{T}(P_t)$ is the traversable mask induced by the local semantics. Let k^* be the feasible candidate ($I_{k^*} = 1$) with lowest soft-risk exposure, and let k_{scaf} be the candidate closest to the geometry-only policy direction. The affordance gate is

$$m_{\text{feas}}(\mathbf{c}, z_t) = \sigma(\kappa_R[(R_{k_{\text{scaf}}} - R_{k^*}) - \rho_R]) \cdot \sigma(\kappa_C(C_{k^*} - \delta_\phi)) \cdot I_{k^*}. \quad (14)$$

Thus m_{feas} activates when: (i) a feasible candidate exists ($I_{k^*} = 1$), (ii) that candidate has clearance above threshold ($C_{k^*} > \delta_\phi$), and (iii) its soft-risk integral is lower than the geometry-only primitive by margin ρ_R . When any condition fails, $m_{\text{feas}} \approx 0$ and F_{soft} is suppressed without affecting F_{hard} .

During one Hamiltonian integration substep m_{feas} is treated as a locally measured context coefficient, exactly like the coefficients predicted from the risk patch. Equivalently, the substep uses local energy $H_{\text{ctx}}^{\text{ra}} = m_{\text{feas}} \lambda_s \tilde{r} + \lambda_h b_{\text{sp}}(\phi)$, with the gate coefficient frozen until the next BEV update.

Implementation notes. The route-aware context-enriched field is not a full-map planner or a global-route oracle. It uses only the local BEV patch, the local SDF, and finite-horizon primitives within the same sensing radius available to all local-sensing baselines. The R1/R2/R3 regime labels are computed externally after the fact to score whether activation was correct; they are not provided to the policy at any time. We use $K=8$, $\delta_\phi=0.15$ m, $\rho_R=0.05$, $\kappa_R=10$, $\kappa_C=20$ in all experiments.

A.4 Coefficient prediction details

The context coefficients (λ_s, λ_h) are predicted by sigmoid-bounded heads from a CNN encoding of the risk patch P_t fused with the existing goal-context token:

$$z_r \leftarrow \psi_\omega(P_t), \quad \lambda_s, \lambda_h \leftarrow \lambda^{\max} \sigma(\text{MLP}(z_r, z_g)), \quad (15)$$

where z_g is the goal-context token from the geometry-only policy and λ^{\max} is a fixed upper bound on each coefficient. The geometric heads (α, β, γ) from the geometry-only policy are frozen, making (λ_s, λ_h) the only route by which context can alter the decision field. This isolation is what makes the constant-coefficient ablation (Table 3, constant-coeff row) interpretable: setting λ_s, λ_h to fixed scalars removes context-sensitivity while keeping the force-channel structure, isolating the contribution of adaptive coefficient prediction.

In highway-env we additionally expose a contextual lateral response coefficient and a TTC-conditioned interaction channel; in boxed traffic the TTC channel suppresses lateral activation while in the open slow-leader case it allows activation. A λ -entropy regularizer L_λ prevents the sigmoid heads from saturating.

A.5 Balanced objective and evaluation metric mapping

The full training objective combines the CVaR tail-risk term with a balanced failure-profile cost:

$$\mathcal{J}_{\text{bal}}(\pi) = \lambda_{\text{goal}}C_{\text{goal}} + \lambda_{\text{risk}}C_{\text{risk}} + \lambda_{\text{barrier}}C_{\text{barrier}} + \lambda_{\text{control}}C_{\text{control}} + \lambda_{\text{smooth}}C_{\text{smooth}} + \lambda_{\text{dyn}}C_{\text{dyn}}, \quad (16)$$

where the dynamic-risk term C_{dyn} is active for interaction domains (highway-env) and zero otherwise. The terms are not optimized independently: low risk by stopping, low control by failing to evade, and short paths through hazards are all failure modes. The context-enriched field learns a context-conditioned compromise among these terms.

The one-to-one mapping from \mathcal{J}_{bal} terms to evaluation metrics is deliberate: goal/progress \rightarrow success, progress, path length; soft risk \rightarrow cumulative risk, soft CVaR; barriers \rightarrow hard-hazard length, off-road events; control/smoothness \rightarrow oscillation, curvature, jerk; dynamic risk \rightarrow clearance, TTC violation, intervention window. The metrics are not post-hoc decorations; they measure the same terms the learned field is balancing.

A.6 Why expected cost is insufficient

Catastrophic contact, collision, or route failure is a tail event: the bulk of rollouts may look acceptable while the failures that determine deployment safety are rare. Expected-cost training is then dominated by typical-case path quality and allocates too little gradient to the rollouts where the new context force channels must become active.

This is not merely a risk-aversion preference. When training under expected cost, the gradient $\partial\mathcal{L}/\partial\lambda_s$ receives contributions from all rollouts, including the majority where $\nabla\tilde{r}$ is small or where no risk-reduction opportunity exists. Gradient signal from safe typical-case rollouts dilutes the signal from the few rollouts where $-\tau\nabla\tilde{r}$ should drive a large λ_s update. CVaR fixes this by restricting gradient to the worst $(1 - \alpha)$ fraction: on those rollouts, $-\tau\nabla\tilde{r}$ contributes non-zero $\partial q_{t+1}/\partial\lambda_s$ at every step, driving λ_s toward values that bias the field away from high-risk regions exactly where the safety signal lives.

The experimental evidence for this is in Table 2: context-enriched expected cost vs. route-aware CVaR. Same architecture, same gate, different objective. CVaR halves false pre-activation (0.370 \rightarrow 0.180), raises suppression rate (0.630 \rightarrow 0.820), and improves navigation success by 30% (0.620 \rightarrow 0.810). The R1-only subset (Table 15) confirms the improvement holds even when an escape genuinely exists, ruling out the explanation that CVaR simply avoids acting.

A.7 Context-enriched update loops and training algorithm

The context-enriched field’s adaptation hierarchy comprises three concurrent loops that operate at different timescales, read different inputs, and update different objects.

Loop 1 – segment (within episode, deployment-time). A rank-1 secant Gauss–Newton corrector adjusts (β, γ) and the top- K nearest α_j between consecutive frames using realized clearance, goal distance, and speed. The Jacobian is maintained as $\hat{J} \leftarrow \mu\hat{J} + (1-\mu)\Delta y\Delta\zeta^\top / \|\Delta\zeta\|^2$ and a damped least-squares step $\Delta\zeta^* = (\hat{J}^\top\hat{J} + \rho I)^{-1}\hat{J}^\top(y_{\text{tgt}} - y)$ is applied with per-coordinate rates and projection to $\mathbb{R}_{\geq 0}$. This loop runs at every simulator step and uses no extra rollouts.

Loop 2 – episode (training-time, between rollouts). Backpropagation through the differentiable rollout integrator against Eq. (7), plus auxiliary losses: imitation to a risk-aware target ($L_{\text{traj}}, L_{\text{vel}}$), multi-start robustness (L_{multi}), clearance penalty (L_{clear}), and λ -entropy regularizer (L_λ). Updates the full parameter vector including θ_R and risk encoder ω .

Loop 3 – curriculum (training-time, between phases). Geometry-backbone weights are loaded from a geometry-only checkpoint with $\lambda_s, \lambda_h \equiv 0$ so $F_{\text{ctx}} \equiv 0$ initially. Imitation weights are reduced to $0.3 \times$ their geometry-only values. A passivity surrogate $\mathcal{L}_{\text{pass}}$ on a held-out window gates phase advancement; the curriculum gradually exposes harder material patches, narrower corridors, stronger hazard penalties, and interaction scenarios.

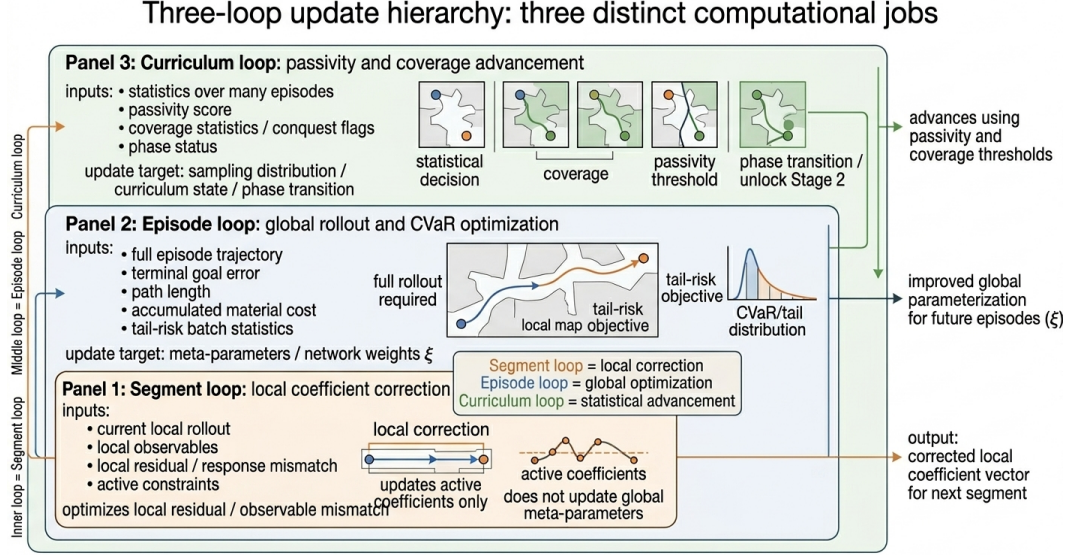


Figure 5: **Three loops as three distinct computational jobs.** The segment loop corrects active coefficients per step. The episode loop optimizes meta-parameters via CVaR. The curriculum loop advances training phases statistically.

A.8 Context-enriched training algorithm

A.9 Energy enrichment induces force and sensitivity channels

Lemma 1 (Energy enrichment induces force, sensitivity, and excitation channels). *Let*

$$H_{\text{enr}}(q, p; \theta, \vartheta) = H_{\text{scaf}}(q, p; \theta) + \vartheta H_{\text{new}}(q),$$

where $H_{\text{new}} \in C^1$ and $\vartheta \in \mathbb{R}$ is a learnable scalar. Then:

1. the enriched momentum equation contains the new force channel

$$F_{\text{new}}(q) = -\vartheta \nabla_q H_{\text{new}}(q);$$

2. differentiating a rollout-dependent loss J through the discrete update creates the direct sensitivity stream

$$\frac{\partial J}{\partial \vartheta} = -\tau \sum_t \left\langle \frac{\partial J}{\partial p_{t+1}}, \nabla_q H_{\text{new}}(q_t) \right\rangle + \text{recursive terms};$$

3. local identifiability of ϑ from force observations requires non-degenerate excitation of the new channel, i.e. the empirical Gram matrix over $\{\nabla_q H_{\text{new}}(q_t)\}_t$ must be nonsingular on the observed force subspace.

Proof. Since

$$\nabla_q H_{\text{enr}} = \nabla_q H_{\text{scaf}} + \vartheta \nabla_q H_{\text{new}},$$

Algorithm 1 Context-aware continual Hamiltonian learning (training; Loops 2 & 3)

Require: geometry-only checkpoint $\theta_{\text{geo}} = (\alpha, \beta, \gamma, \theta_R)$; dataset \mathcal{D} of short rollouts with local context patches; CVaR level $\alpha_c=0.95$; batch size B ; horizon H ; step τ .

Loop 3 – backward-compatible geometry-only \rightarrow context-enriched initialization.

- 1: $\theta_{\text{enr}} \leftarrow \theta_{\text{scaf}}$; initialize risk encoder ω and heads so $\lambda_s, \lambda_h \equiv 0$ at output $\triangleright F_{\text{ctx}} \equiv 0$ initially
- 2: Reduce imitation weights $(w_{\text{traj}}, w_{\text{vel}}) \leftarrow 0.3(w_{\text{traj}}, w_{\text{vel}})$
- 3: **for** epoch $e = 1, \dots, E$ **do**
 - Loop 2 – episode loop (one minibatch).**
 - 4: **for** minibatch $\{(q_0^{(i)}, p_0^{(i)}, q_g^{(i)}, \mathcal{O}^{(i)}, P^{(i)}, H^{(i)})\}_{i=1}^B \in \mathcal{D}$ **do**
 - 5: $(\alpha^{(i)}, \beta^{(i)}, \gamma^{(i)}) \leftarrow \phi_{\text{geom}}(\mathcal{O}^{(i)}, q_g^{(i)} - q_0^{(i)})$ \triangleright geometry transformer, unchanged from geometry-only policy
 - 6: $z_r^{(i)} \leftarrow \psi_\omega(P^{(i)})$; $\lambda_s^{(i)}, \lambda_h^{(i)} \leftarrow \lambda^{\max} \sigma(\text{MLP}(z_r^{(i)}, z_g^{(i)}))$
 - 7: **for** $t = 0, \dots, H^{(i)} - 1$ (differentiable rollout) **do**
 - 8: $(\tilde{r}_t, \phi_t, \nabla \tilde{r}_t, \nabla \phi_t) \leftarrow \text{BilinearSample}(P^{(i)}, q_t^{(i)})$ \triangleright resample at *current* q , not q_0
 - 9: $m_{\text{feas}} \leftarrow \text{LocalGate}(P^{(i)}, q_t^{(i)}, q_g^{(i)})$ \triangleright Eq. (5); set to 1 for scalar context-enriched field
 - 10: $F_{\text{soft}} \leftarrow -m_{\text{feas}} \lambda_s^{(i)} \nabla \tilde{r}_t$; $F_{\text{hard}} \leftarrow -\lambda_h^{(i)} b'_{\text{sp}}(\phi_t) \nabla \phi_t$ \triangleright Eq. (4)
 - 11: $p_{t+1}^{(i)} \leftarrow p_t^{(i)} + \tau(F_{\text{geom}} + F_{\text{soft}} + F_{\text{hard}}) - \tau \gamma^{(i)} M^{-1} p_t^{(i)}$ $\triangleright R_\theta = \gamma M^{-1} p$; $M=I$ in implementation
 - 12: $q_{t+1}^{(i)} \leftarrow q_t^{(i)} + \tau M^{-1} p_{t+1}^{(i)}$
 - 13: Accumulate cum_risk, hard_count, arc
 - 14: **end for**
 - 15: $J^{(i)} \leftarrow \text{Eq. (6)}$
 - 16: $\hat{\eta} \leftarrow \widehat{Q}_{\alpha_c}(\{J^{(i)}\}_{i=1}^B)$ \triangleright empirical quantile, **detach from graph**
 - 17: $\widehat{\text{CVaR}}_{\alpha_c} \leftarrow \hat{\eta} + \frac{1}{(1-\alpha_c)B} \sum_i (J^{(i)} - \hat{\eta})_+$ \triangleright Eq. (7); gradient flows only through tail rollouts
 - 18: $\mathcal{L} \leftarrow \widehat{\text{CVaR}}_{\alpha_c} + \sum_k w_k L_k$ $\triangleright L_k \in \{L_{\text{traj}}, L_{\text{vel}}, L_{\text{fric}}, L_{\text{clear}}, L_{\text{multi}}, L_\lambda\}$
 - 19: $\theta_{\text{enr}} \leftarrow \theta_{\text{enr}} - \text{lr} \nabla_{\theta_{\text{enr}}} \mathcal{L}$, $\|\nabla\|_2$ clipped to 5.0
 - 20: **end for**
 - Loop 3 – curriculum advancement check.**
 - 21: Compute passivity surrogate $\mathcal{L}_{\text{pass}}$ on validation window
 - 22: **if** violation rate $< \eta_{\text{tol}}$ over last W epochs **then**
 - 23: Mark phase as advanced; optionally widen risk-class distribution in \mathcal{D}
 - 24: **end if**
 - 25: **end for**
 - 26: **return** θ_{enr}

Hamilton’s momentum equation contains

$$-\nabla_q H_{\text{enr}} = -\nabla_q H_{\text{scaf}} - \vartheta \nabla_q H_{\text{new}}.$$

Thus the added term contributes the force channel $F_{\text{new}} = -\vartheta \nabla_q H_{\text{new}}$.

For the sensitivity statement, consider the discrete momentum update

$$p_{t+1} = p_t - \tau \nabla_q H_{\text{scaf}}(q_t, p_t) - \tau \vartheta \nabla_q H_{\text{new}}(q_t) + \dots$$

Differentiating with respect to ϑ gives

$$\frac{\partial p_{t+1}}{\partial \vartheta} = \frac{\partial p_t}{\partial \vartheta} - \tau \nabla_q H_{\text{new}}(q_t) - \tau \nabla_q^2 H_{\text{enr}}(q_t, p_t) \frac{\partial q_t}{\partial \vartheta} + \dots$$

Applying the chain rule to any rollout loss J yields

$$\frac{\partial J}{\partial \vartheta} = \sum_t \left\langle \frac{\partial J}{\partial p_{t+1}}, \frac{\partial p_{t+1}}{\partial \vartheta} \right\rangle + \sum_t \left\langle \frac{\partial J}{\partial q_{t+1}}, \frac{\partial q_{t+1}}{\partial \vartheta} \right\rangle.$$

The displayed direct stream is the term produced by $-\tau \nabla_q H_{\text{new}}(q_t)$; the remaining terms are recursive contributions through $\partial q_t / \partial \vartheta$ and $\partial p_t / \partial \vartheta$.

For identifiability, suppose two coefficients ϑ, ϑ' induce the same observed force on the rollout. Then

$$(\vartheta - \vartheta') \nabla_q H_{\text{new}}(q_t) = 0$$

in all observed force directions. A nonzero coefficient difference is impossible only when the observed gradients span the relevant force subspace. Equivalently, the corresponding empirical Gram matrix is nonsingular on that subspace. \square

A.10 Force-dictionary separation

Lemma 2 (Context forces cannot be obtained by geometric reweighting). *Let the geometry-only force dictionary at q be*

$$\mathcal{D}_{\text{geom}}(q) = \text{span}\{\nabla_q D_{\mathcal{G}}(q), \nabla_q b_{\text{IPC}}(d_1(q)), \dots, \nabla_q b_{\text{IPC}}(d_N(q))\}.$$

If $P_{\mathcal{D}^\perp} \nabla_q \tilde{r}(q) \neq 0$, then there is no choice of geometry-only coefficient reweighting that reproduces $F_{\text{soft}} = -\lambda_s \nabla_q \tilde{r}(q)$ for $\lambda_s \neq 0$.

Proof. Any geometry-only coefficient reweighting remains in $\mathcal{D}_{\text{geom}}(q)$. But F_{soft} has nonzero projection onto $\mathcal{D}_{\text{geom}}(q)^\perp$ whenever $\lambda_s P_{\mathcal{D}^\perp} \nabla_q \tilde{r}(q) \neq 0$, so it cannot equal any vector in the geometry-only span. \square

A.11 Passivity and practical discrete dissipativity

Theorem 1 (Contextual Hamiltonian enrichment preserves dissipativity). *Under Assumptions 1–3, if the context z is fixed and $u = 0$, then along solutions of (9)–(10),*

$$\frac{d}{dt} H_{\text{enr}}(q(t), p(t); z) = -v(t)^\top D(q(t), p(t); z) v(t) \leq -\rho \|v(t)\|^2 \leq 0.$$

Thus the addition of H_{ctx} preserves the port-Hamiltonian dissipativity structure. If $z = z(t)$ and $u \neq 0$, then

$$\frac{d}{dt} H_{\text{enr}} = -v^\top Dv + \langle \nabla_z H_{\text{ctx}}(q; z), \dot{z} \rangle + \langle \nabla_p H_{\text{enr}}, Bu \rangle.$$

Hence the enriched system is passive with storage H_{enr} and supply rate

$$s(t) = \langle \nabla_z H_{\text{ctx}}(q; z), \dot{z} \rangle + \langle \nabla_p H_{\text{enr}}, Bu \rangle.$$

Proof. For fixed z , differentiate H_{enr} along trajectories:

$$\dot{H}_{\text{enr}} = \langle \nabla_q H_{\text{enr}}, \dot{q} \rangle + \langle \nabla_p H_{\text{enr}}, \dot{p} \rangle.$$

Using $\dot{q} = \nabla_p H_{\text{enr}}$ and $\dot{p} = -\nabla_q H_{\text{enr}} - D\nabla_p H_{\text{enr}}$, we obtain

$$\dot{H}_{\text{enr}} = \langle \nabla_q H_{\text{enr}}, \nabla_p H_{\text{enr}} \rangle + \langle \nabla_p H_{\text{enr}}, -\nabla_q H_{\text{enr}} - D\nabla_p H_{\text{enr}} \rangle.$$

The two interconnection terms cancel:

$$\langle \nabla_q H_{\text{enr}}, \nabla_p H_{\text{enr}} \rangle - \langle \nabla_p H_{\text{enr}}, \nabla_q H_{\text{enr}} \rangle = 0.$$

Therefore

$$\dot{H}_{\text{enr}} = -\langle \nabla_p H_{\text{enr}}, D\nabla_p H_{\text{enr}} \rangle.$$

Since $\nabla_p H_{\text{enr}} = M^{-1}p = v$,

$$\dot{H}_{\text{enr}} = -v^\top Dv.$$

By Assumption 3, $D \succeq \rho I$, so

$$-v^\top Dv \leq -\rho \|v\|^2 \leq 0.$$

If $z = z(t)$, the chain rule adds

$$\langle \nabla_z H_{\text{enr}}, \dot{z} \rangle = \langle \nabla_z H_{\text{ctx}}, \dot{z} \rangle.$$

If $u \neq 0$, the input term Bu in \dot{p} contributes

$$\langle \nabla_p H_{\text{enr}}, Bu \rangle.$$

Combining these terms gives the claimed supply-rate identity. \square

Theorem 2 (Practical discrete dissipativity and step-size condition). *Under Assumptions 1–3, let $u_t = 0$. For the semi-implicit context-enriched update (11)–(12), there exists a finite constant $C_{\mathcal{K}} > 0$ such that*

$$H_{\text{enr}}(x_{t+1}; z_t) - H_{\text{enr}}(x_t; z_t) \leq -\tau v_t^\top D_t v_t + C_{\mathcal{K}} \tau^2.$$

Consequently, the discrete rollout is practically dissipative. If

$$\tau < \frac{v_t^\top D_t v_t}{C_{\mathcal{K}}},$$

then $H_{\text{enr}}(x_{t+1}; z_t) < H_{\text{enr}}(x_t; z_t)$. If $v_t^\top D_t v_t \geq d_{\min} > 0$ uniformly on a region of interest, then any

$$\tau < \frac{d_{\min}}{C_{\mathcal{K}}}$$

guarantees one-step energy decrease on that region.

Proof. Let $f_z(x)$ be the continuous-time vector field defined by (9)–(10) with $u = 0$. Since the semi-implicit update is a first-order consistent discretization of this vector field and all derivatives are bounded on compact \mathcal{K} , there exists $C_I > 0$ such that

$$x_{t+1} = x_t + \tau f_{z_t}(x_t) + e_t, \quad \|e_t\| \leq C_I \tau^2.$$

Because $H_{\text{enr}} \in C^2(\mathcal{K})$, its gradient is Lipschitz. Let L_H be a Lipschitz constant for ∇H_{enr} . The smoothness inequality gives

$$H_{\text{enr}}(x_{t+1}) - H_{\text{enr}}(x_t) \leq \langle \nabla H_{\text{enr}}(x_t), x_{t+1} - x_t \rangle + \frac{L_H}{2} \|x_{t+1} - x_t\|^2.$$

Substituting $x_{t+1} - x_t = \tau f_{z_t}(x_t) + e_t$,

$$\begin{aligned} H_{\text{enr}}(x_{t+1}) - H_{\text{enr}}(x_t) &\leq \tau \langle \nabla H_{\text{enr}}(x_t), f_{z_t}(x_t) \rangle + \langle \nabla H_{\text{enr}}(x_t), e_t \rangle \\ &\quad + \frac{L_H}{2} \|\tau f_{z_t}(x_t) + e_t\|^2. \end{aligned}$$

By Theorem 1,

$$\langle \nabla H_{\text{enr}}(x_t), f_{z_t}(x_t) \rangle = -v_t^\top D_t v_t.$$

The remaining two terms are bounded by $C_{\mathcal{K}} \tau^2$ for some finite constant $C_{\mathcal{K}}$, since \mathcal{K} is compact and $\|\nabla H_{\text{enr}}\|$, $\|f_z\|$, and $\|e_t\|/\tau^2$ are bounded there. Hence

$$H_{\text{enr}}(x_{t+1}; z_t) - H_{\text{enr}}(x_t; z_t) \leq -\tau v_t^\top D_t v_t + C_{\mathcal{K}} \tau^2.$$

Strict decrease follows whenever $C_{\mathcal{K}} \tau^2 < \tau v_t^\top D_t v_t$. Dividing by $\tau > 0$ yields the step-size condition. The uniform-margin result follows by replacing $v_t^\top D_t v_t$ by d_{\min} . \square

A.12 Geometry-only preservation and no-hallucination

Theorem 3 (Geometry-only preservation under small context force). *Let $x_t^{\text{geo}} = (q_t^{\text{geo}}, p_t^{\text{geo}})$ be the geometry-only rollout and $x_t^{\text{enr}} = (q_t^{\text{enr}}, p_t^{\text{enr}})$ be the context-enriched rollout, initialized from the same state, and suppose Assumptions 1, 2, and 4 hold. If along the rollout tube*

$$\|\nabla_q H_{\text{ctx}}(q; z)\| \leq \varepsilon.$$

Then after N steps,

$$\|x_N^{\text{enr}} - x_N^{\text{geo}}\| \leq \tau \sqrt{1 + \tau^2} \|M^{-1}\|^2 \varepsilon \frac{(1 + \tau L_\Phi)^N - 1}{\tau L_\Phi},$$

with the last factor interpreted as N when $L_\Phi = 0$. In particular, if $\varepsilon = 0$, the context-enriched rollout recovers the geometry-only rollout up to numerical roundoff.

Proof. The only difference between the geometry-only and context-enriched fields is the context term in the momentum update. At one step, this perturbation is

$$\delta p_{t+1} = -\tau \nabla_q H_{\text{ctx}}(q_t; z_t),$$

and the induced position perturbation is

$$\delta q_{t+1} = \tau M^{-1} \delta p_{t+1} = -\tau^2 M^{-1} \nabla_q H_{\text{ctx}}(q_t; z_t).$$

Thus

$$\|\delta p_{t+1}\| \leq \tau \varepsilon, \quad \|\delta q_{t+1}\| \leq \tau^2 \|M^{-1}\| \varepsilon.$$

The one-step state perturbation is therefore bounded by

$$\|\delta x_{t+1}\| \leq \tau \sqrt{1 + \tau^2 \|M^{-1}\|^2} \varepsilon.$$

Let

$$e_t = \|x_t^{\text{enr}} - x_t^{\text{geo}}\|.$$

By Assumption 4,

$$e_{t+1} \leq (1 + \tau L_\Phi) e_t + \tau \sqrt{1 + \tau^2 \|M^{-1}\|^2} \varepsilon.$$

Since $e_0 = 0$, iterating gives

$$e_N \leq \tau \sqrt{1 + \tau^2 \|M^{-1}\|^2} \varepsilon \sum_{j=0}^{N-1} (1 + \tau L_\Phi)^j.$$

Evaluating the geometric sum yields the result. \square

Corollary 1 (No hallucinated lateral escape). *Let P_\perp denote projection onto the lateral subspace. Suppose local coordinates are baseline-aligned so that longitudinal context forces do not generate lateral motion to first order. If*

$$\|P_\perp \nabla_q H_{\text{ctx}}(q; z)\| \leq \varepsilon_\perp$$

on the rollout tube, then

$$\|P_\perp (q_N^{\text{enr}} - q_N^{\text{geo}})\| \leq C_{\perp, N} \varepsilon_\perp,$$

where

$$C_{\perp, N} = \tau^2 \|P_\perp M^{-1} P_\perp^\top\| \frac{(1 + \tau L_\Phi)^N - 1}{\tau L_\Phi}.$$

When $\varepsilon_\perp = 0$, the context channel cannot produce a lateral escape.

Proof. Project the context-induced position perturbation:

$$P_\perp \delta q_{t+1} = -\tau^2 P_\perp M^{-1} \nabla_q H_{\text{ctx}}(q_t; z_t).$$

Under baseline-aligned local coordinates, the first-order longitudinal–lateral cross terms vanish, so

$$\|P_\perp \delta q_{t+1}\| \leq \tau^2 \|P_\perp M^{-1} P_\perp^\top\| \varepsilon_\perp.$$

Propagating this one-step projected perturbation through the same Lipschitz recursion as in Theorem 3 gives the claimed bound. \square

A.13 Selective risk deflection and risk reduction

Theorem 4 (Selective risk deflection and local risk reduction). *Let P_\perp project onto a feasible lateral subspace. Suppose that at a state q ,*

$$\|P_\perp \nabla_q \tilde{r}(\mathbf{c}; z)\| \geq \Delta,$$

and suppose the projected hard-hazard force does not cancel the soft-risk direction by more than χ :

$$\|P_\perp [\lambda_h b'_{\text{sp}}(\phi(\mathbf{c}; z)) \nabla_q \phi(\mathbf{c}; z)]\| \leq \chi.$$

Then

$$\|P_\perp F_{\text{ctx}}(q; z)\| \geq \lambda_s \Delta - \chi.$$

Thus, whenever $\lambda_s \Delta > \chi$, the context channel is necessarily active in the lateral subspace.

Assume further that \tilde{r} has L_r -Lipschitz gradient, $M^{-1} \succeq m_M I$, and

$$\tau^2 \lambda_s \|M^{-1}\| \leq \frac{1}{L_r}.$$

Then, ignoring shared geometry and dissipation terms up to $O(\tau^3)$, the one-step context-enriched perturbation satisfies

$$\tilde{r}(q_{t+1}^{\text{enr}}) - \tilde{r}(q_{t+1}^{\text{scaf}}) \leq -\frac{1}{2}\tau^2\lambda_s m_M \Delta^2 + O(\tau^3).$$

Over any active window \mathcal{A} on which the same margin condition holds,

$$\sum_{t \in \mathcal{A}} [\tilde{r}(q_{t+1}^{\text{enr}}) - \tilde{r}(q_{t+1}^{\text{scaf}})] \leq -\frac{1}{2}|\mathcal{A}|\tau^2\lambda_s m_M \Delta^2 + O(|\mathcal{A}|\tau^3).$$

Proof. The context force is

$$F_{\text{ctx}} = -\lambda_s \nabla_q \tilde{r} - \lambda_h b'_{\text{sp}}(\phi) \nabla_q \phi.$$

Projecting onto the lateral subspace gives

$$P_{\perp} F_{\text{ctx}} = -\lambda_s P_{\perp} \nabla_q \tilde{r} - P_{\perp} [\lambda_h b'_{\text{sp}}(\phi) \nabla_q \phi].$$

By the reverse triangle inequality,

$$\|P_{\perp} F_{\text{ctx}}\| \geq \lambda_s \|P_{\perp} \nabla_q \tilde{r}\| - \|P_{\perp} [\lambda_h b'_{\text{sp}}(\phi) \nabla_q \phi]\|.$$

The assumptions imply

$$\|P_{\perp} F_{\text{ctx}}\| \geq \lambda_s \Delta - \chi.$$

This proves activation under $\lambda_s \Delta > \chi$.

For the risk-reduction claim, isolate the soft-risk force

$$F_{\text{soft}} = -\lambda_s \nabla_q \tilde{r}(q).$$

The position perturbation induced by this force in one semi-implicit step is

$$\delta q = -\tau^2 \lambda_s M^{-1} \nabla_q \tilde{r}(q).$$

By L_r -smoothness,

$$\tilde{r}(q + \delta q) \leq \tilde{r}(q) + \langle \nabla_q \tilde{r}(q), \delta q \rangle + \frac{L_r}{2} \|\delta q\|^2.$$

The first-order term is

$$\langle \nabla_q \tilde{r}(q), \delta q \rangle = -\tau^2 \lambda_s \nabla_q \tilde{r}(q)^{\top} M^{-1} \nabla_q \tilde{r}(q).$$

Since $M^{-1} \succeq m_M I$ and $\|\nabla_q \tilde{r}(q)\| \geq \Delta$ on the active projected direction,

$$\nabla_q \tilde{r}(q)^{\top} M^{-1} \nabla_q \tilde{r}(q) \geq m_M \Delta^2.$$

Therefore

$$\langle \nabla_q \tilde{r}(q), \delta q \rangle \leq -\tau^2 \lambda_s m_M \Delta^2.$$

The second-order term is

$$\frac{L_r}{2} \|\delta q\|^2 = \frac{L_r}{2} \tau^4 \lambda_s^2 \|M^{-1} \nabla_q \tilde{r}(q)\|^2.$$

The step-size condition

$$\tau^2 \lambda_s \|M^{-1}\| \leq \frac{1}{L_r}$$

ensures that this second-order term is controlled by the first-order decrease, yielding

$$\tilde{r}(q + \delta q) - \tilde{r}(q) \leq -\frac{1}{2}\tau^2 \lambda_s m_M \Delta^2.$$

The shared geometry and dissipative terms are identical in the geometry-only and context-enriched fields local comparison; by smoothness, their contribution to the relative risk difference is $O(\tau^3)$. Summing the one-step inequality over \mathcal{A} proves the final claim. \square

A.14 CVaR gradient consistency

The episode cost used in the main text is

$$J(\theta) = w_g \|q_T - q_g\|^2 + w_\ell \sum_t \|q_{t+1} - q_t\| + w_r \sum_t \tilde{r}(q_t) \|q_{t+1} - q_t\| + w_h \sum_t \mathbf{1}\{\phi(q_t) < \epsilon\}.$$

The training objective uses the Rockafellar–Uryasev representation of CVaR:

$$\text{CVaR}_\alpha(J_\theta) = \min_{\eta \in \mathbb{R}} \left[\eta + \frac{1}{1-\alpha} \mathbb{E}(J_\theta - \eta)_+ \right].$$

Theorem 5 (Detached empirical CVaR gives a consistent tail-gradient estimator). *Let $J_\theta(\xi)$ be the rollout cost induced by parameter θ and rollout randomness ξ . Fix $\alpha \in (0, 1)$. Assume:*

1. $J_\theta(\xi)$ is differentiable in θ almost surely;
2. $\|\nabla_\theta J_\theta(\xi)\| \leq G$ almost surely;
3. the distribution of J_θ has a continuous density near its α -quantile;
4. $\mathbb{P}[J_\theta = \eta_\alpha(\theta)] = 0$, where $\eta_\alpha(\theta) = \text{VaR}_\alpha(J_\theta)$.

Then

$$\nabla_\theta \text{CVaR}_\alpha(J_\theta) = \frac{1}{1-\alpha} \mathbb{E}[\nabla_\theta J_\theta(\xi) \mathbf{1}\{J_\theta(\xi) \geq \eta_\alpha(\theta)\}].$$

Given B i.i.d. rollouts and the detached empirical quantile

$$\hat{\eta} = \widehat{Q}_\alpha(\{J_\theta^{(i)}\}_{i=1}^B),$$

define

$$\hat{g}_B(\theta) = \frac{1}{(1-\alpha)B} \sum_{i=1}^B \nabla_\theta J_\theta^{(i)} \mathbf{1}\{J_\theta^{(i)} \geq \hat{\eta}\}.$$

Then

$$\hat{g}_B(\theta) \rightarrow \nabla_\theta \text{CVaR}_\alpha(J_\theta)$$

almost surely as $B \rightarrow \infty$, and

$$\|\hat{g}_B(\theta) - \nabla_\theta \text{CVaR}_\alpha(J_\theta)\| = O_p(B^{-1/2}).$$

If $J_\theta \in [0, J_{\max}]$, then the empirical CVaR value obeys

$$|\widehat{\text{CVaR}}_\alpha - \text{CVaR}_\alpha| = O\left(\frac{J_{\max}}{1-\alpha} \sqrt{\frac{\log(1/\delta)}{B}}\right)$$

with probability at least $1 - \delta$.

Proof. The Rockafellar–Uryasev variational form gives

$$\text{CVaR}_\alpha(J_\theta) = \min_{\eta \in \mathbb{R}} \left[\eta + \frac{1}{1-\alpha} \mathbb{E}(J_\theta - \eta)_+ \right].$$

At the minimizer,

$$\eta^* = \eta_\alpha(\theta).$$

By the envelope theorem, when differentiating the optimized value with respect to θ , the derivative of the optimizer $\eta^*(\theta)$ does not appear. Hence

$$\nabla_\theta \text{CVaR}_\alpha(J_\theta) = \frac{1}{1-\alpha} \nabla_\theta \mathbb{E}[(J_\theta - \eta^*)_+].$$

Since J_θ is differentiable almost surely and the quantile boundary has probability zero,

$$\nabla_\theta (J_\theta - \eta^*)_+ = \nabla_\theta J_\theta \mathbf{1}\{J_\theta \geq \eta^*\}$$

almost surely. The bounded-gradient assumption permits interchanging derivative and expectation, proving

$$\nabla_{\theta} \text{CVaR}_{\alpha}(J_{\theta}) = \frac{1}{1-\alpha} \mathbb{E}[\nabla_{\theta} J_{\theta} \mathbf{1}\{J_{\theta} \geq \eta_{\alpha}\}].$$

For the empirical estimator, continuity of the distribution near η_{α} implies strong consistency of the empirical quantile:

$$\hat{\eta} \rightarrow \eta_{\alpha}$$

almost surely. Since there is no atom at the quantile,

$$\mathbf{1}\{J_{\theta}^{(i)} \geq \hat{\eta}\} \rightarrow \mathbf{1}\{J_{\theta}^{(i)} \geq \eta_{\alpha}\}$$

almost surely. The summands are bounded by $G/(1-\alpha)$, so dominated convergence and the strong law of large numbers give

$$\hat{g}_B(\theta) \rightarrow \frac{1}{1-\alpha} \mathbb{E}[\nabla_{\theta} J_{\theta} \mathbf{1}\{J_{\theta} \geq \eta_{\alpha}\}] = \nabla_{\theta} \text{CVaR}_{\alpha}(J_{\theta})$$

almost surely.

For the rate, decompose

$$\hat{g}_B - g = A_B + R_B,$$

where

$$A_B = \frac{1}{(1-\alpha)B} \sum_{i=1}^B [\nabla J_i \mathbf{1}\{J_i \geq \eta_{\alpha}\} - \mathbb{E}(\nabla J \mathbf{1}\{J \geq \eta_{\alpha}\})]$$

and

$$R_B = \frac{1}{(1-\alpha)B} \sum_{i=1}^B \nabla J_i [\mathbf{1}\{J_i \geq \hat{\eta}\} - \mathbf{1}\{J_i \geq \eta_{\alpha}\}].$$

The first term is a bounded empirical average, so $A_B = O_p(B^{-1/2})$. The second term is nonzero only when J_i lies between $\hat{\eta}$ and η_{α} . The probability mass of this interval is $O_p(|\hat{\eta} - \eta_{\alpha}|)$, and standard empirical quantile theory gives $|\hat{\eta} - \eta_{\alpha}| = O_p(B^{-1/2})$. Hence $R_B = O_p(B^{-1/2})$, proving the gradient rate.

For bounded J_{θ} , the empirical Rockafellar–Uryasev objective is a bounded empirical process indexed by η . Uniform concentration over $\eta \in [0, J_{\max}]$, followed by comparison at the empirical and population minimizers, yields the displayed

$$O\left(\frac{J_{\max}}{1-\alpha} \sqrt{\frac{\log(1/\delta)}{B}}\right)$$

concentration rate. □

A.15 Risk-averse constrained OCP interpretation

This subsection formalizes the statement that the contextual Hamiltonian should be viewed as an amortized approximation to a *family* of risk-averse constrained optimal control problems, not as an unconditional online optimizer. The Hamiltonian policy is a structured feedback parameterization, while the constrained OCP is the reference problem whose local Lagrangian force field it aims to approximate.

Consider a finite-horizon controlled system

$$x_{t+1} = \Phi(x_t, u_t, z_t), \quad x_t = (q_t, p_t), \quad t = 0, \dots, H-1, \quad (17)$$

with local context process z_t and rollout randomness ξ . Let $J_0(\tau)$ denote the nominal goal, path-length, smoothness, and control-effort cost. Let $C_j(\tau)$ denote the exposure accumulated by risk channel j , for example soft-material exposure, hard-hazard proximity, deformation risk, or interaction risk. The risk-averse constrained reference family is

$$\begin{aligned} \min_{\pi \in \Pi} \quad & \mathbb{E}[J_0(\tau_{\pi})] \\ \text{s.t.} \quad & \text{CVaR}_{\alpha_j}(C_j(\tau_{\pi})) \leq \bar{p}_j, \quad j = 1, \dots, m. \end{aligned} \quad (18)$$

Equivalently, for nonnegative multipliers $\lambda \in \mathbb{R}_+^m$, its Lagrangian risk objective is

$$\mathcal{J}_\lambda(\pi) = \mathbb{E}[J_0(\tau_\pi)] + \sum_{j=1}^m \lambda_j (\text{CVaR}_{\alpha_j}(C_j(\tau_\pi)) - \bar{\rho}_j). \quad (19)$$

Under a local constraint qualification, a locally optimal constrained policy admits KKT multipliers [Shapiro et al., 2009] λ^* ; the corresponding first-order conditions are those of (19) at λ^* together with complementary slackness. This is the precise sense in which the coefficients of risk-aware energy terms can be interpreted as local risk prices.

The learned Hamiltonian policy class is

$$H_\theta(q, p; z) = \frac{1}{2} p^\top M^{-1} p + U_\theta(q, z), \quad u_{\text{raw}} = \pi_\theta(x, z), \quad (20)$$

where the induced closed-loop vector field has the form

$$F_\theta(x, z) = (J - R_\theta) \nabla_x H_\theta(x, z) + G(x) u_{\text{raw}}. \quad (21)$$

The next theorem states the approximation claim used in the main text. It is a local inverse-optimality statement: if the Hamiltonian force approximates the local optimal Lagrangian closed-loop force, then the resulting trajectories and risk-Lagrangian values are close.

Theorem 6 (Hamiltonian approximation of the risk-averse Lagrangian OCP). *Fix a compact rollout tube \mathcal{K} and a multiplier vector $\lambda \in \mathbb{R}_+^m$. Suppose that a locally optimal feedback π_λ^* for (19) induces a closed-loop update map Φ_λ^* on \mathcal{K} , and the Hamiltonian feedback π_θ induces a closed-loop update map Φ_θ . Assume:*

1. Φ_λ^* is L_Φ -Lipschitz on \mathcal{K} ;
2. the one-step model mismatch is uniformly bounded,

$$\sup_{x, z \in \mathcal{K}} \|\Phi_\theta(x, z) - \Phi_\lambda^*(x, z)\| \leq \varepsilon_\Phi; \quad (22)$$

3. the rollout costs J_0, C_1, \dots, C_m are $L_J, L_{C_1}, \dots, L_{C_m}$ Lipschitz functions of the finite trajectory under the sup norm.

Then trajectories initialized at the same x_0 satisfy

$$\max_{0 \leq t \leq H} \|x_t^\theta - x_t^*\| \leq C_H \varepsilon_\Phi, \quad C_H := \sum_{k=0}^{H-1} (1 + L_\Phi)^k. \quad (23)$$

Moreover,

$$\mathcal{J}_\lambda(\pi_\theta) - \mathcal{J}_\lambda(\pi_\lambda^*) \leq \left(L_J + \sum_{j=1}^m \lambda_j L_{C_j} \right) C_H \varepsilon_\Phi. \quad (24)$$

If the constrained problem (18) satisfies a local constraint qualification and λ^* is a KKT multiplier at a local constrained solution, then (24) applies to the local Lagrangian relaxation of the constrained risk-averse OCP at λ^* .

Proof. Let $e_t = x_t^\theta - x_t^*$. By adding and subtracting $\Phi_\lambda^*(x_t^\theta, z_t)$,

$$\begin{aligned} \|e_{t+1}\| &\leq \|\Phi_\theta(x_t^\theta, z_t) - \Phi_\lambda^*(x_t^\theta, z_t)\| + \|\Phi_\lambda^*(x_t^\theta, z_t) - \Phi_\lambda^*(x_t^*, z_t)\| \\ &\leq \varepsilon_\Phi + (1 + L_\Phi) \|e_t\|. \end{aligned}$$

Since $e_0 = 0$, discrete Gronwall gives

$$\max_{0 \leq t \leq H} \|e_t\| \leq \varepsilon_\Phi \sum_{k=0}^{H-1} (1 + L_\Phi)^k = C_H \varepsilon_\Phi.$$

The Lipschitz assumptions on the trajectory functionals imply

$$|J_0(\tau_\theta) - J_0(\tau_*)| \leq L_J C_H \varepsilon_\Phi, \quad |C_j(\tau_\theta) - C_j(\tau_*)| \leq L_{C_j} C_H \varepsilon_\Phi.$$

CVaR is monotone and translation equivariant. Therefore, if two random variables X, Y obey $|X - Y| \leq a$ almost surely, then $|\text{CVaR}_\alpha(X) - \text{CVaR}_\alpha(Y)| \leq a$. Applying this with $X = C_j(\tau_\theta)$, $Y = C_j(\tau_\star)$ and $a = L_{C_j} C_H \varepsilon_\Phi$ gives

$$|\text{CVaR}_{\alpha_j}(C_j(\tau_\theta)) - \text{CVaR}_{\alpha_j}(C_j(\tau_\star))| \leq L_{C_j} C_H \varepsilon_\Phi.$$

Combining the nominal and risk-channel bounds yields (24). Finally, under the stated constraint qualification, the KKT conditions identify the local constrained solution with a stationary point of the Lagrangian relaxation at some nonnegative multiplier λ^\star satisfying complementary slackness; substituting $\lambda = \lambda^\star$ gives the constrained-OCP interpretation. \square

A.16 Identifiability, generalization, and upper-confidence risk safety

This subsection makes precise what can and cannot be identified from learning the risk-aware Hamiltonian, and how the empirical CVaR update becomes a genuine risk-constraint update once an upper-confidence radius is added. The argument uses three standard ingredients: uniform convergence for bounded function classes via Rademacher complexity [Bartlett and Mendelson, 2002, Shalev-Shwartz and Ben-David, 2014], quantile/CVaR concentration via the Dvoretzky–Kiefer–Wolfowitz inequality with Massart’s constant [Dvoretzky et al., 1956, Massart, 1990], and forward-invariance of barrier-filtered dynamics via Nagumo/CBF conditions [Nagumo, 1942, Ames et al., 2017].

Structured risk-energy class. For a local context patch z , write the learned potential as

$$U_\theta(q, z) = U_{\text{goal}}(q, z) + \sum_{i=1}^{N(z)} \alpha_i(z) B_i(q, z) + U_{\text{res}, \theta}(q, z), \quad (25)$$

where B_i are fixed differentiable obstacle or risk-barrier atoms and $U_{\text{res}, \theta}$ is the learned residual shaping potential. The induced force is

$$F_\theta(q, z) = -\nabla_q U_\theta(q, z). \quad (26)$$

The scalar potential is never identifiable beyond an additive constant; only its gradient can be identified from local force or direction observations. Moreover, the split between the structured barrier part and the residual is identifiable only under an excitation and non-absorption condition.

Assumption 5 (Barrier excitation and residual non-absorption). For each context patch z , let

$$G_B(q, z) = [\nabla_q B_1(q, z), \dots, \nabla_q B_{N(z)}(q, z)] \in \mathbb{R}^{d \times N(z)}.$$

There exists $\kappa_B > 0$ such that

$$\lambda_{\min}(\mathbb{E}_{q \sim \mu_z} [G_B(q, z)^\top G_B(q, z)]) \geq \kappa_B. \quad (27)$$

The residual force is either constrained to be small, $\mathbb{E}_{\mu_z} \|\nabla_q U_{\text{res}, \theta}\|^2 \leq \varepsilon_{\text{res}}^2$, or orthogonal to the barrier dictionary,

$$\mathbb{E}_{q \sim \mu_z} [G_B(q, z)^\top \nabla_q U_{\text{res}, \theta}(q, z)] = 0. \quad (28)$$

Proposition 2 (Local identifiability of the structured risk weights). *Fix z and suppose the teacher force admits the decomposition*

$$F^\star(q, z) = -\nabla_q U_{\text{goal}}(q, z) - G_B(q, z) \alpha^\star(z) + \epsilon(q, z), \quad (29)$$

with $\mathbb{E} \|\epsilon(q, z)\|^2 \leq \sigma_\epsilon^2$. Let $\hat{\alpha}(z)$ minimize the population least-squares force error over the structured class with residual either removed or constrained as in Assumption 5. Then

$$\|\hat{\alpha}(z) - \alpha^\star(z)\| \leq \frac{1}{\kappa_B} \left(\|\mathbb{E}[G_B(q, z)^\top \epsilon(q, z)]\| + \varepsilon_{\text{res}} \sqrt{\mathbb{E} \|G_B(q, z)\|_{\text{op}}^2} \right). \quad (30)$$

In particular, if the model is well specified, the residual is orthogonal to the barrier dictionary, and $\mathbb{E}[G_B^\top \epsilon] = 0$, then $\hat{\alpha}(z) = \alpha^\star(z)$. Without the Gram condition (27), the structured weights are not identifiable.

Proof. Subtract $-\nabla U_{\text{goal}}$ from both the teacher force and the model force. The population normal equation for the structured coefficients is

$$\mathbb{E}[G_B^\top G_B] \hat{\alpha} = \mathbb{E}[G_B^\top (G_B \alpha^\star - \epsilon - r_\theta)],$$

where $r_\theta = \nabla_q U_{\text{res},\theta}$, with the sign absorbed consistently in both sides. Hence

$$\mathbb{E}[G_B^\top G_B](\hat{\alpha} - \alpha^*) = -\mathbb{E}[G_B^\top \epsilon] - \mathbb{E}[G_B^\top r_\theta].$$

Taking norms and using $\|A^{-1}\|_{\text{op}} \leq 1/\kappa_B$ gives

$$\|\hat{\alpha} - \alpha^*\| \leq \frac{1}{\kappa_B} (\|\mathbb{E}[G_B^\top \epsilon]\| + \|\mathbb{E}[G_B^\top r_\theta]\|).$$

If the residual is orthogonal to the dictionary, the second term vanishes. If it is only small, Cauchy–Schwarz gives

$$\|\mathbb{E}[G_B^\top r_\theta]\| \leq \sqrt{\mathbb{E}\|G_B\|_{\text{op}}^2} \sqrt{\mathbb{E}\|r_\theta\|^2} \leq \varepsilon_{\text{res}} \sqrt{\mathbb{E}\|G_B\|_{\text{op}}^2}.$$

This proves the bound. If $\mathbb{E}[G_B^\top G_B]$ is singular, there exists a nonzero vector a in its nullspace. Then $G_B(q, z)a = 0$ for μ_z -almost every q , so α and $\alpha + a$ induce the same observed structured force. Thus the coefficients are not identifiable. \square

Assumption 6 (Bounded force class). Let

$$\mathcal{F} = \{(q, p, z) \mapsto F_\theta(q, p, z) : \theta \in \Theta\}$$

be the force class induced by the Hamiltonian network on the compact rollout tube \mathcal{K} . Assume that $\|F_\theta(q, p, z) - F^*(q, p, z)\| \leq M_F$ and that the squared loss class

$$\mathcal{L}_F = \{(q, p, z, F^*) \mapsto \|F_\theta(q, p, z) - F^*\|^2 : \theta \in \Theta\}$$

is measurable and has empirical Rademacher complexity $\mathfrak{R}_n(\mathcal{L}_F)$.

Theorem 7 (Force-field generalization). *Let $(q_i, p_i, z_i, F_i^*)_{i=1}^n$ be i.i.d. samples from the local patch distribution, and define*

$$\mathcal{R}_F(\theta) = \mathbb{E}\|F_\theta(q, p, z) - F^*(q, p, z)\|^2, \quad \widehat{\mathcal{R}}_{F,n}(\theta) = \frac{1}{n} \sum_{i=1}^n \|F_\theta(q_i, p_i, z_i) - F_i^*\|^2.$$

Under Assumption 6, with probability at least $1 - \delta$,

$$\mathcal{R}_F(\hat{\theta}) \leq \widehat{\mathcal{R}}_{F,n}(\hat{\theta}) + 2\mathfrak{R}_n(\mathcal{L}_F) + 3M_F^2 \sqrt{\frac{\log(2/\delta)}{2n}} \quad (31)$$

for every data-dependent estimator $\hat{\theta} \in \Theta$. If the learned dynamics and costs are Lipschitz on \mathcal{K} , this force error propagates to rollout-cost error with a finite-horizon Gronwall factor.

Proof. The first statement is the standard Rademacher uniform convergence inequality for a bounded loss class [Bartlett and Mendelson, 2002, Shalev-Shwartz and Ben-David, 2014]: with probability at least $1 - \delta$,

$$\sup_{\theta \in \Theta} (\mathcal{R}_F(\theta) - \widehat{\mathcal{R}}_{F,n}(\theta)) \leq 2\mathfrak{R}_n(\mathcal{L}_F) + 3M_F^2 \sqrt{\frac{\log(2/\delta)}{2n}}.$$

Substituting the random estimator $\hat{\theta}$ into this uniform event gives (31). For the rollout statement, let $e_t = x_t^\theta - x_t^*$. If the closed-loop update map is L_Φ -Lipschitz and the one-step force mismatch is bounded by ε_F , then

$$\|e_{t+1}\| \leq (1 + \tau L_\Phi) \|e_t\| + \tau \varepsilon_F.$$

Iterating gives

$$\max_{0 \leq t \leq H} \|e_t\| \leq \tau \varepsilon_F \sum_{k=0}^{H-1} (1 + \tau L_\Phi)^k.$$

Lipschitz continuity of the finite-horizon cost then converts the trajectory bound into an objective bound. \square

Lemma 3 (Upper-confidence CVaR bound). *Let $C(\tau_\theta) \in [0, C_{\max}]$ be a bounded rollout risk exposure and let C_1, \dots, C_B be i.i.d. validation rollouts for a fixed policy θ . Define the population and empirical Rockafellar–Uryasev objectives*

$$\varphi(\eta) = \eta + \frac{1}{1-\alpha} \mathbb{E}[(C - \eta)_+], \quad (32)$$

$$\widehat{\varphi}_B(\eta) = \eta + \frac{1}{(1-\alpha)B} \sum_{i=1}^B (C_i - \eta)_+. \quad (33)$$

Let

$$\rho_\alpha = \inf_{\eta \in \mathbb{R}} \varphi(\eta), \quad \widehat{\rho}_{\alpha, B} = \inf_{\eta \in \mathbb{R}} \widehat{\varphi}_B(\eta).$$

Then, with probability at least $1 - \delta$,

$$\rho_\alpha \leq \widehat{\rho}_{\alpha, B} + \frac{C_{\max}}{1-\alpha} \sqrt{\frac{\log(2/\delta)}{2B}}. \quad (34)$$

For m bounded risk channels $C_j \in [0, C_{j, \max}]$, the bound holds simultaneously for all channels with probability at least $1 - \delta$ after using

$$\beta_{j, B}(\delta/m) := \frac{C_{j, \max}}{1-\alpha_j} \sqrt{\frac{\log(2m/\delta)}{2B}}. \quad (35)$$

Proof. Because $C \in [0, C_{\max}]$, every minimizer of φ and $\widehat{\varphi}_B$ may be chosen in $[0, C_{\max}]$: if $\eta < 0$, increasing η to 0 cannot increase the Rockafellar–Uryasev objective, and if $\eta > C_{\max}$, decreasing η to C_{\max} cannot increase it. Hence it is enough to control the objectives uniformly over $\eta \in [0, C_{\max}]$.

Let F and F_B denote the population and empirical distribution functions of C . For $\eta \in [0, C_{\max}]$, the tail-integral identity gives

$$\mathbb{E}[(C - \eta)_+] = \int_{\eta}^{C_{\max}} (1 - F(t)) dt, \quad \frac{1}{B} \sum_{i=1}^B (C_i - \eta)_+ = \int_{\eta}^{C_{\max}} (1 - F_B(t)) dt. \quad (36)$$

Therefore, for every $\eta \in [0, C_{\max}]$,

$$|\widehat{\varphi}_B(\eta) - \varphi(\eta)| \leq \frac{1}{1-\alpha} \int_{\eta}^{C_{\max}} |F_B(t) - F(t)| dt \quad (37)$$

$$\leq \frac{C_{\max}}{1-\alpha} \|F_B - F\|_{\infty}. \quad (38)$$

Massart’s sharp form of the Dvoretzky–Kiefer–Wolfowitz inequality states that [Dvoretzky et al., 1956, Massart, 1990]

$$\mathbb{P}(\|F_B - F\|_{\infty} > \epsilon) \leq 2 \exp(-2B\epsilon^2). \quad (39)$$

Thus, with probability at least $1 - \delta$,

$$\|F_B - F\|_{\infty} \leq \sqrt{\frac{\log(2/\delta)}{2B}}.$$

Combining this event with (38) gives

$$\sup_{\eta \in [0, C_{\max}]} |\widehat{\varphi}_B(\eta) - \varphi(\eta)| \leq \frac{C_{\max}}{1-\alpha} \sqrt{\frac{\log(2/\delta)}{2B}}. \quad (40)$$

Finally, for any two functions f, g , $|\inf f - \inf g| \leq \sup |f - g|$. Applying this with $f = \varphi$ and $g = \widehat{\varphi}_B$ on the event (40) yields

$$\rho_\alpha \leq \widehat{\rho}_{\alpha, B} + \frac{C_{\max}}{1-\alpha} \sqrt{\frac{\log(2/\delta)}{2B}}.$$

The simultaneous result follows by applying the same argument to each channel with failure probability δ/m and taking a union bound. \square

Theorem 8 (Upper-confidence risk-constrained learning). *For each risk channel $j = 1, \dots, m$, let*

$$\rho_j(\theta) = \text{CVaR}_{\alpha_j}(C_j(\tau_\theta)), \quad \widehat{\rho}_{j,B}(\theta) = \widehat{\text{CVaR}}_{\alpha_j,B}(C_j(\tau_\theta)) + \beta_{j,B}(\delta/m),$$

where $\beta_{j,B}$ is chosen as in Eq. (35). Let $\hat{\theta}$ be fixed before drawing the validation rollouts used to compute $\widehat{\rho}_{j,B}$; alternatively, let $\beta_{j,B}$ include a uniform function-class complexity term. If

$$\widehat{\rho}_{j,B}(\hat{\theta}) \leq \bar{\rho}_j, \quad j = 1, \dots, m, \quad (41)$$

then, with probability at least $1 - \delta$,

$$\rho_j(\hat{\theta}) \leq \bar{\rho}_j, \quad j = 1, \dots, m. \quad (42)$$

Moreover, the projected dual update

$$\lambda_j^{k+1} = [\lambda_j^k + \eta_\lambda(\widehat{\rho}_{j,B}(\theta_k) - \bar{\rho}_j)]_+ \quad (43)$$

performs ascent on the empirical upper-bound Lagrangian constraint violation and therefore increases the risk price exactly when the upper-confidence budget is violated.

Proof. Because the validation rollouts are independent of the fixed iterate $\hat{\theta}$, Lemma 3 applies to that iterate. A union bound over the m risk channels implies that, with probability at least $1 - \delta$,

$$\rho_j(\hat{\theta}) \leq \widehat{\rho}_{j,B}(\hat{\theta})$$

holds simultaneously for all j . Combining this event with (41) gives

$$\rho_j(\hat{\theta}) \leq \widehat{\rho}_{j,B}(\hat{\theta}) \leq \bar{\rho}_j,$$

which proves true risk feasibility. The dual statement follows because the Lagrangian term for channel j is $\lambda_j(\widehat{\rho}_{j,B}(\theta) - \bar{\rho}_j)$ with the constraint $\lambda_j \geq 0$; projected gradient ascent in λ_j is exactly (43). \square

Theorem 9 (Optional CBF projection condition). *Let*

$$\mathcal{S} = \{x : \bar{R}_j(x, z) \leq \bar{\rho}_j, j = 1, \dots, m\}$$

where each \bar{R}_j is continuously differentiable in x for fixed z . Suppose that, at every $x \in \mathcal{S}$, the online filter chooses a feasible input u satisfying

$$\nabla_x \bar{R}_j(x, z)^\top (f(x) + G(x)u) \leq -\kappa_j(\bar{R}_j(x, z) - \bar{\rho}_j), \quad j = 1, \dots, m, \quad (44)$$

with $\kappa_j > 0$. Then \mathcal{S} is forward invariant for the filtered continuous-time closed-loop dynamics. If the optional port-power constraint $y^\top u \leq \delta$ is also included and the filter remains feasible, the same invariance conclusion holds with the additional passivity budget enforced pointwise.

Proof. Define $h_j(x, z) = \bar{\rho}_j - \bar{R}_j(x, z)$. The safe set is $\mathcal{S} = \{x : h_j(x, z) \geq 0, j = 1, \dots, m\}$. Condition (44) is equivalent to

$$\dot{h}_j(x, z) = -\nabla_x \bar{R}_j(x, z)^\top (f(x) + G(x)u) \geq \kappa_j(\bar{R}_j(x, z) - \bar{\rho}_j) = -\kappa_j h_j(x, z).$$

By the comparison lemma, if $h_j(0) \geq 0$, then $h_j(t) \geq e^{-\kappa_j t} h_j(0) \geq 0$ for all times on which the solution exists. Equivalently, no trajectory starting in \mathcal{S} can cross a boundary $h_j = 0$ outward. This is the standard Nagumo/CBF forward-invariance argument [Nagumo, 1942, Ames et al., 2017]. Adding $y^\top u \leq \delta$ only further restricts the feasible input set; if feasibility is preserved, the already-imposed inequalities continue to imply invariance. \square

A.17 Barrier caveat: finite barriers are not CBF certificates

The hard-hazard term $b_{\text{sp}}(\phi)$ is a differentiable repulsive barrier. It should not be stated as a formal forward-invariance certificate unless an additional condition is imposed. In continuous time, forward invariance follows if the barrier diverges at the unsafe boundary and total energy is bounded. In discrete time, one needs either a sufficiently small step size that prevents crossing between samples, or an explicit control-barrier-function projection/filter satisfying a discrete or continuous CBF condition [Ames et al., 2017]. The optional projection theorem above states such a sufficient condition, but the empirical Stage 2 results in this paper use the Hamiltonian risk field without claiming a formal CBF certificate. Therefore, our main claims are geometry-only preservation, dissipativity, selectivity, and local empirical risk reduction under stated regularity assumptions; they are not unconditional collision-avoidance guarantees.

A.18 Empirical checks for the selectivity consequences

The theory statements above are used as falsifiable rollout predictions, not as unconditional safety certificates. Table 7 states the condition, the corresponding empirical measurement, and where it is tested. The preservation bound in Theorem 3 predicts that small context force yields small deviation from the geometry-only rollout. Table 8 reports the finite-rollout version of this check at the same deviation threshold used in the experiments.

Table 7: **Theory-to-metric checks.** Each theoretical consequence is paired with an empirical statistic in the main experiments. The paper reports these as measured rollout behavior, not as a formal invariance certificate.

Consequence	Checkable prediction	Empirical test
C1: geometry-only preservation	If $\ F_{\text{ctx}}\ $ is small, trajectory deviation from the geometry-only rollout is small.	R3 preservation / low pre-escape deviation; measured through false pre-activation and suppression rate in Table 2.
C2: no hallucinated escape	If $P_{\perp} F_{\text{ctx}}$ is small in blocked regimes, lateral escape attempts are rare.	RELLIS static FAR and delayed-required false pre-activation (Tables 3, 2).
C3: risk deflection	If a feasible lower-risk direction has positive projected margin, the context force aligns with it and risk exposure decreases after activation.	RELLIS static CAR/SR/AUPRC and delayed-required success/CVaR (Tables 3, 2).

Table 8: **Empirical geometry-only deviation check for Theorem 3.** The theorem gives $\|P_{\perp}(q_t - q_t^{\text{geo}})\| \leq C_{\perp, N} \varepsilon_{\perp}$. The experiments instantiate this as a thresholded rollout check: when the projected context force is suppressed, lateral deviation from the geometry-only rollout should stay below the measured reaction threshold δ .

Rollout condition	Bound prediction	Observed below- δ	Failure metric
Geometry-only policy, delayed escape	$\varepsilon_{\perp} = 0 \Rightarrow$ no context deviation	1.000	false pre-act 0.000
Route-aware Ctx, static R2	suppressed $P_{\perp} F_{\text{ctx}} \Rightarrow$ no hallucinated escape	0.886	FAR 0.114
Route-aware Ctx CVaR, pre-escape delayed	pre-escape suppression \Rightarrow no early lateral deviation	0.820	false pre-act 0.180

B Additional Experimental Results

This appendix preserves the broader diagnostic tables and qualitative panels while keeping the main paper focused on the selectivity signature.

B.1 DFC2018 Full Planner Comparison

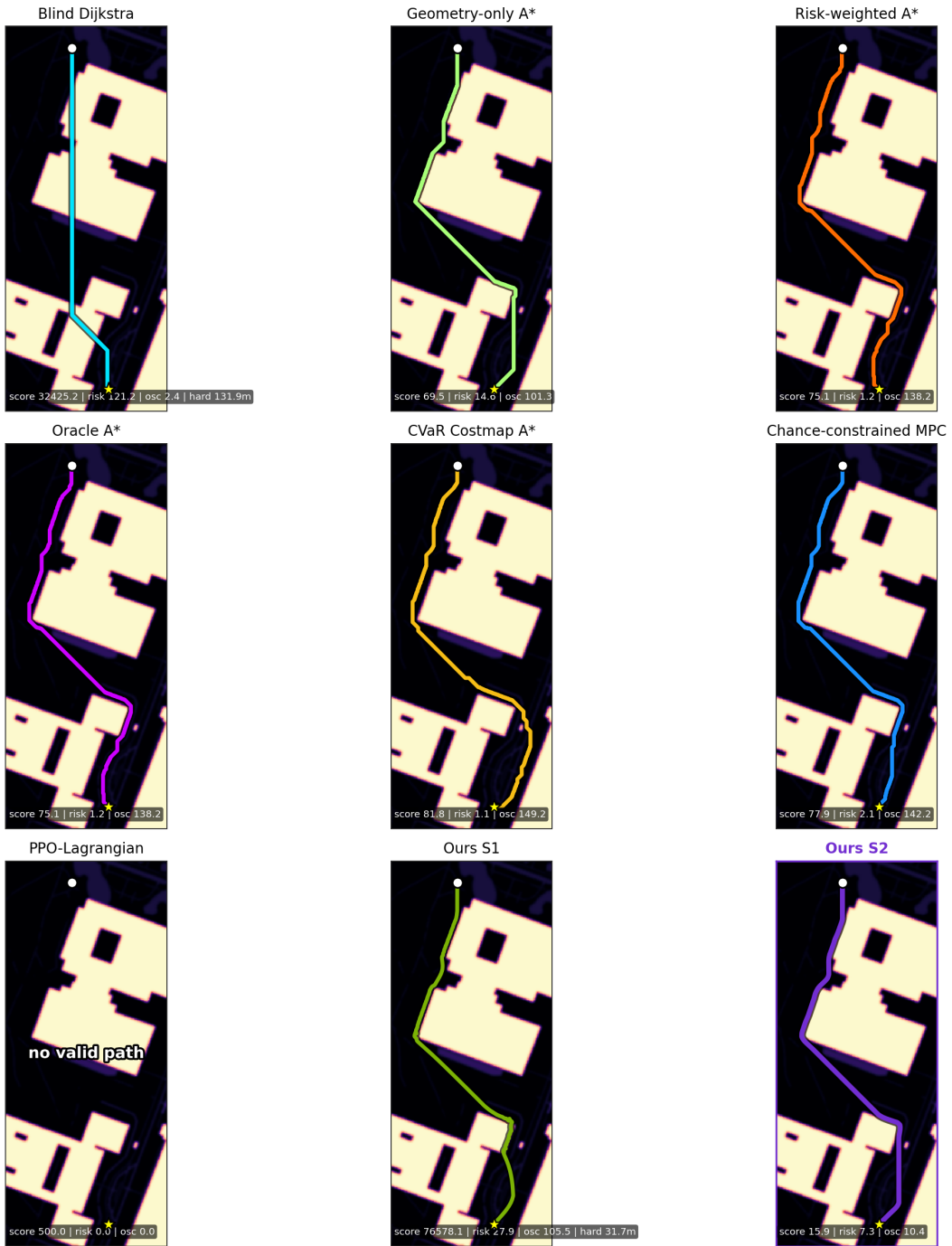
Table 9 reports the full DFC2018 comparison including privileged full-map planners. The interpretation is unchanged from the main text: full-map planners with global access obtain lower raw static risk, but context-enriched field substantially repairs the geometry-only policy while producing smoother continuous trajectories and zero oscillation. PPO-Lagrangian fails to find a valid path on 20% of episodes.

B.2 RELLIS-3D Cross-Sequence Details

Table 11 reports the full six-method spatial selectivity table with fold standard errors over five leave-one-sequence-out splits and adds AUPRC. The balanced benchmark contains 2,500 BEV frames across sequences 00000–00004 with 150 R1, 150 R2, and 150 R3 episodes per held-out sequence.

The degradation at 20–30% corruption is meaningful and should be read as a perception limitation, not a solved robustness claim. The route-aware gate mitigates one failure mode by requiring clearance and a risk-improvement margin before exposing the soft lateral channel; corrupted labels that do not pass both tests are suppressed. It does not repair the risk map online, so systematic semantic errors

DFC episode 0124: separate path choices by method



White circle = start, yellow star = goal. Red tint marks hard-risk terrain; magma brightness marks soft-risk intensity.

Figure 6: **Independent DFC path panels (episode 0124)**. Each panel shows one method’s trajectory on the same episode. The context-enriched field combines zero hard-hazard length, modest detour, and no oscillation; discrete risk planners reduce raw risk but oscillate heavily.

Table 9: **DFC2018 full evaluation.** Means over 300 paired test episodes. Oracle A* is privileged (global map access) and serves as a reference ceiling, not a fair local-sensing competitor.

Method	Success \uparrow	Cat. fail \downarrow	Hard len. \downarrow	Risk \downarrow	Risk/m \downarrow	Len. ratio	Osc. \downarrow	Fail score \downarrow
Blind Dijkstra	1.000	0.967	55.386	55.292	0.244	1.000	1.990	12927.5
Geometry-only A*	1.000	0.033	0.576	10.365	0.042	1.069	24.819	164.5
Risk-weighted A*	1.000	0.033	0.333	3.753	0.014	1.106	54.480	127.0
Oracle A* \dagger	1.000	0.000	0.000	3.664	0.014	1.169	58.512	37.2
CVaR costmap A*	1.000	0.033	0.287	3.318	0.012	1.143	72.780	120.8
Chance-constrained MPC	1.000	0.033	0.287	4.171	0.016	1.116	58.957	114.0
PPO-Lagrangian	0.800	0.233	0.355	3.753	0.014	1.104	13.221	200.3
Ours geometry-only policy	0.867	0.600	21.106	23.267	0.099	1.044	82.212	53216.6
Ours ctx-enriched	1.000	0.100	0.658	9.493	0.039	1.045	7.629	115.8

Table 10: **DFC failure-mode breakdown.** Episode fractions. Risk planners reduce raw material cost but frequently introduce discrete oscillation; the context-enriched field primarily repairs the learned geometry policy.

Method	No path	Hard haz.	High soft risk	Excess detour	Osc.
Blind Dijkstra	0.00	0.97	0.97	0.00	0.00
Geometry A*	0.00	0.03	0.20	0.07	0.43
Risk-weighted A*	0.00	0.03	0.07	0.10	0.83
CVaR costmap A*	0.00	0.03	0.07	0.17	0.90
Chance-const. MPC	0.00	0.03	0.07	0.07	0.83
PPO-Lagrangian	0.20	0.23	0.10	0.13	0.23
Ours geometry-only policy	0.13	0.60	0.63	0.00	0.63
Ours ctx-enriched	0.00	0.10	0.40	0.03	0.00

can still reduce CAR and increase FAR. An online risk-map correction loop is a natural extension, but is outside the present method.

B.3 RELIS-Dyn: Full Event Breakdown

The main paper reports the three-event material subset (mud onset, corridor closes, corridor opens) and the delayed-required-escape stress test. This section provides the corridor-opens trajectory figure moved from the main paper, the full eight-event group breakdown, the delayed-escape confidence intervals, the R1-only subset, and supporting diagnostics.

Corridor-opens trajectory (dynamic R1). Figure 8 shows the dynamic R1 case in detail. When the blocked corridor becomes traversable at t_{event} , The context-enriched field updates F_{ctx} from the new BEV patch in the same integration step and enters the lower-risk route immediately. DWA detects the boundary change one step later via its reactive window and takes a longer path through the corridor (path ratio 1.151 vs. 0.982 for the context-enriched field on the selected episode). The bottom trace quantifies the stale-exposure gap: soft-risk accumulated between t_{event} and first lateral deviation from the pre-event geometry-only trajectory.

Delayed-required-escape: bootstrap CIs. Table 14 gives paired bootstrap 95% confidence intervals for the main delayed-required-escape table (100 episodes, 10,000 resamples). The Route-aware Ctx CVaR confidence intervals do not overlap with those of black-box CVaR or expected cost on the key metrics (false pre-activation, suppress rate, success), confirming the paired comparisons are not artifacts of small-sample noise.

R1-only subset. Table 15 reports the delayed-required-escape results restricted to episodes where a feasible escape exists throughout ($n=44$, i.e. episodes where t_{escape} is early enough that the escape is open for at least half the remaining horizon). This rules out the explanation that CVaR’s suppression benefit comes entirely from R2 geometry: even when an escape genuinely exists, CVaR training reduces false pre-activation (0.445 vs. 0.545) and improves success (0.736 vs. 0.655).

Table 11: **RELLIS-3D spatial selectivity, full six-method table.** Mean \pm fold standard error over five leave-one-sequence-out splits. Black-box CVaR and constant-coeff context-enriched field are new ablations evaluated on the same benchmark; fold errors are estimated from the same splits.

Method	CAR \uparrow	FAR \downarrow	SR \uparrow	AUPRC \uparrow
Geometry-only policy	0.000 \pm 0.000	0.000 \pm 0.000	0.000 \pm 0.000	0.000 \pm 0.000
Scalar context field	0.378 \pm 0.035	0.752 \pm 0.039	1.031 \pm 0.224	0.008 \pm 0.004
Fixed-coeff context field	0.566 \pm 0.041	0.888 \pm 0.032	1.123 \pm 0.189	0.008 \pm 0.003
Non-route directional Ctx	0.135 \pm 0.015	0.178 \pm 0.025	1.165 \pm 0.168	0.206 \pm 0.037
Black-box CVaR policy	0.884 \pm 0.028	0.129 \pm 0.029	1.292 \pm 0.156	0.206 \pm 0.038
Route-aware Ctx	0.837 \pm 0.031	0.114 \pm 0.027	2.358 \pm 0.203	0.289 \pm 0.044

Table 12: **RELLIS-3D behavioral outcomes.** Means over paired local BEV episodes. Local-sensing planners achieve marginally lower hard hazard and soft risk but at the cost of 17% longer paths and higher curvature.

Method	Success \uparrow	Hard haz. \downarrow	Soft risk \downarrow	CVaR risk \downarrow	Path ratio	Curv. \downarrow	Stuck \downarrow
Geometry-only policy	0.86	0.42	21.8	0.78	1.00	12.4	0.11
Risk-loss-only	0.91	0.31	18.7	0.65	1.07	11.5	0.08
Scalar context field	0.92	0.28	18.2	0.63	1.06	10.9	0.08
Non-route directional Ctx	0.90	0.19	18.9	0.61	1.03	10.4	0.09
Route-aware Ctx	0.96	0.12	16.6	0.49	1.05	8.9	0.04
Local risk A*/MPC/MPPI	0.97	0.09	15.8	0.47	1.17	18.6	0.03

Eight-event group summary. Table 16 reports the full eight-event benchmark. The ‘‘Ctx wins?’’ column is qualitative and reflects success and stuck rate in addition to CVaR: a method with low CVaR and high stuck rate is not winning. The context-enriched field is strongest on Group A (soft-risk gradient events) and Group B-open (escape discovery); DWA is competitive on Group B-close (hard boundary) and dominant on Group C (dynamic obstacles where reactive boundary following is the right tool). Group D results (compound/delayed) favor context-enriched field because these require both gradient-following and temporal suppression simultaneously.

Reaction delay threshold sensitivity. Table 17 shows that the corridor-opens reaction delay comparison is stable across three values of the lateral displacement threshold δ used to define reaction. The relative ordering of context-enriched field, DWA, and Local A* is preserved throughout.

Eight-event group Pareto. Figure 9 shows each method’s position on the reaction delay vs. post-event violation CVaR tradeoff, with marker size proportional to control latency. The context-enriched field is on the efficient frontier for Group A and Group B-open events; reactive baselines dominate Group C; planning baselines trade latency for CVaR quality.

Force-channel decomposition. Figure 10 shows mean proxy magnitudes of F_{soft} and F_{hard} across the eight event types. Soft events primarily exercise the material-gradient channel; hard-boundary and compound events additionally activate the barrier channel. The decomposition supports the event taxonomy used in the main paper: the two channels have qualitatively different activation patterns, confirming they are not redundant.

B.4 Highway-env Broad Baselines

Table 18 reports the full highway comparison across 13 methods. MOBIL-IDM is the strongest domain-engineered controller. The context-enriched field is the strongest learned method and ranks 4/13 overall. The main paper’s mechanism ablation (Table 6) explains the activation/suppression behavior; this table provides the broader competitive context.

Table 13: **RELLIS perception robustness.** Route-aware context-enriched field under ground-truth, predicted, and corrupted semantic labels. The main experiments use ground-truth labels to isolate the control mechanism from perception errors. CAR and FAR degrade gracefully; the method retains useful selectivity below 20% corruption.

Semantic input	CAR \uparrow	FAR \downarrow	CVaR risk \downarrow	Success \uparrow
Ground-truth semantics	0.837	0.114	0.49	0.96
Predicted semantics	0.791	0.148	0.53	0.94
10% label corruption	0.769	0.163	0.56	0.93
20% label corruption	0.714	0.218	0.62	0.90
30% label corruption	0.641	0.301	0.74	0.89

Table 14: **Delayed-required-escape: paired bootstrap 95% CIs.** 100 episodes, 10,000 bootstrap resamples.

Method	False pre-act	Suppress	Success	Viol. CVaR
Geometry-only policy	0.000 [0.000, 0.000]	1.000 [1.000, 1.000]	0.030 [0.001, 0.059]	1.894 [1.812, 1.976]
Risk-loss-only	0.420 [0.322, 0.518]	0.580 [0.482, 0.678]	0.040 [0.007, 0.073]	1.793 [1.718, 1.868]
Fixed-coeff context field	0.990 [0.971, 1.000]	0.010 [0.000, 0.029]	0.030 [0.001, 0.059]	0.463 [0.441, 0.485]
Black-box CVaR	0.920 [0.876, 0.964]	0.080 [0.036, 0.124]	0.200 [0.119, 0.281]	0.503 [0.474, 0.532]
DWA semantic	0.950 [0.914, 0.986]	0.050 [0.014, 0.086]	0.480 [0.381, 0.579]	0.695 [0.657, 0.733]
MPPI semantic	0.950 [0.900, 0.990]	0.050 [0.010, 0.100]	0.240 [0.160, 0.330]	0.831 [0.700, 0.975]
Ctx-enriched, expected cost	0.370 [0.273, 0.467]	0.630 [0.533, 0.727]	0.620 [0.523, 0.717]	0.855 [0.819, 0.891]
Route-aware Ctx CVaR	0.180 [0.103, 0.257]	0.820 [0.743, 0.897]	0.810 [0.731, 0.889]	0.740 [0.704, 0.776]

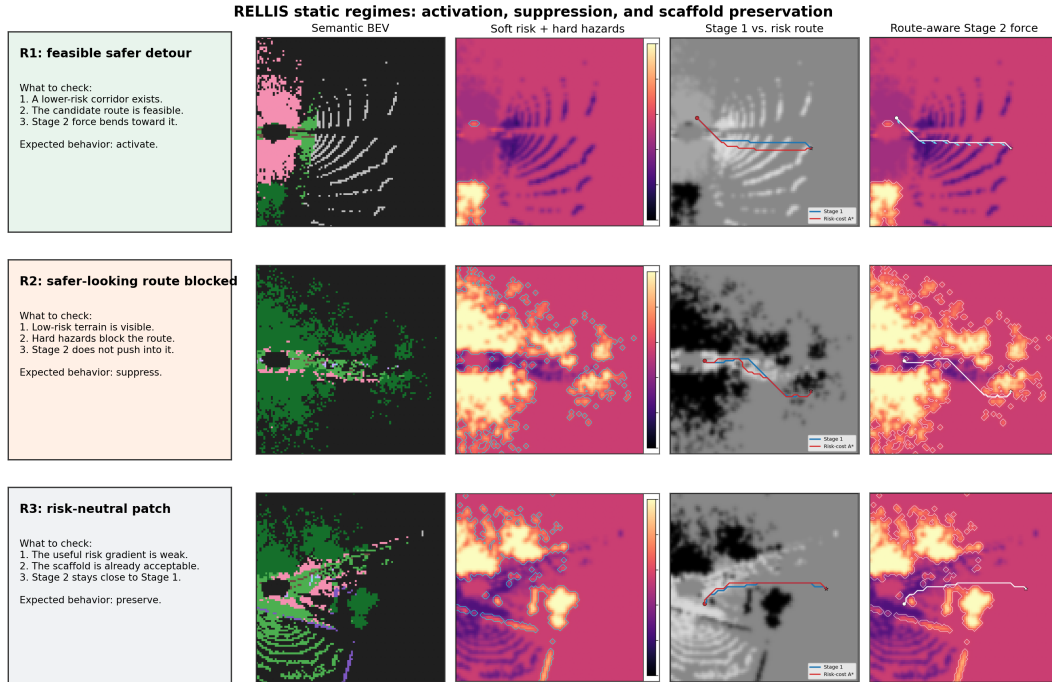


Figure 7: **RELLIS static regime panels.** Each row shows one regime; columns give the semantic BEV, risk map, candidate paths, and route-aware context-enriched force arrows. R1: force bends toward the feasible lower-risk detour. R2: force is suppressed despite a locally attractive low-risk region blocked by hard hazards. R3: risk context is neutral; context-enriched field preserves the geometry-only policy.

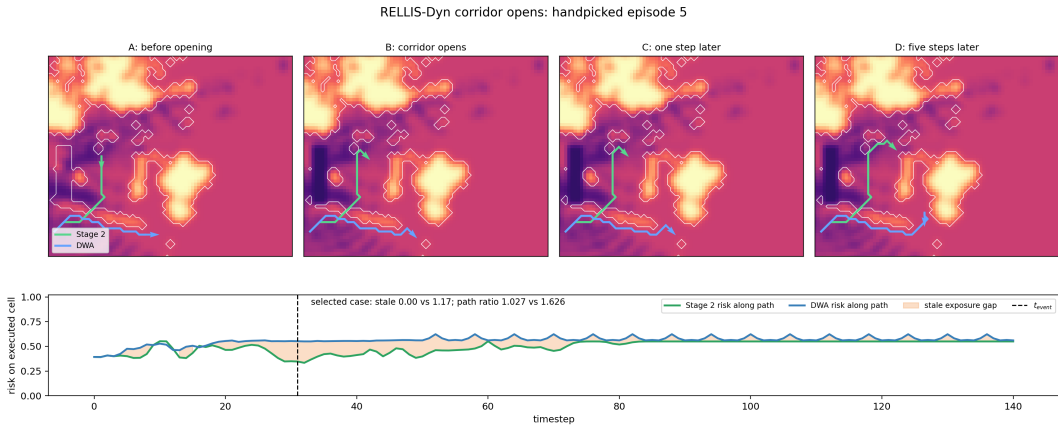


Figure 8: **RELLIS-Dyn corridor opens (dynamic R1)**. A blocked low-risk corridor becomes feasible at t_{event} . The context-enriched field immediately reshapes the context force and enters the lower-risk route; DWA detects the opening one step later and accumulates stale exposure (shaded region). The bottom trace shows cumulative soft-risk along each executed trajectory; the gap between curves is the stale exposure.

Table 15: **R1-only subset of delayed-required-escape ($n=44$)**. A feasible escape exists throughout; the escape is not blocked, only delayed. CVaR reduces premature activation even in the unambiguous R1 setting.

Method	False pre-act↓	Suppress↑	Success↑	Viol. CVaR↓
Ctx-enriched, expected cost	0.545	0.455	0.655	0.848
Route-aware Ctx CVaR	0.445	0.555	0.736	0.717

Table 16: **RELLIS-Dyn 8-event group summary**. Reaction delay and post-event CVaR by event group. “Ctx wins?” reflects success, stuck, and CVaR jointly.

Group	Event	Ctx delay↓	DWA delay↓	Ctx CVaR↓	DWA CVaR↓	Ctx wins?
A-soft	mud onset	8.2	2.8	0.853	0.688	yes
A-soft	puddle expansion	7.9	2.5	0.664	0.610	yes
B-hard	corridor closes	7.2	3.4	0.588	0.551	mixed
B-hard	corridor opens	5.1	2.3	0.561	0.539	yes
C-dyn	crossing obstacle	8.2	3.2	0.561	0.560	no
C-dyn	moving obs. blocks	5.7	4.0	0.743	0.601	no
D-comp	mud + blocked detour	7.3	2.7	0.898	0.712	yes
D-comp	delayed escape opens	5.6	2.2	0.859	0.664	yes

Table 17: **Reaction delay sensitivity to δ** (corridor-opens, 100 episodes).

δ (m)	context-enriched field↓	DWA↓	Local A*↓
0.10	5.3	2.5	4.8
0.15	5.1	2.3	4.6
0.20	4.8	2.1	4.3

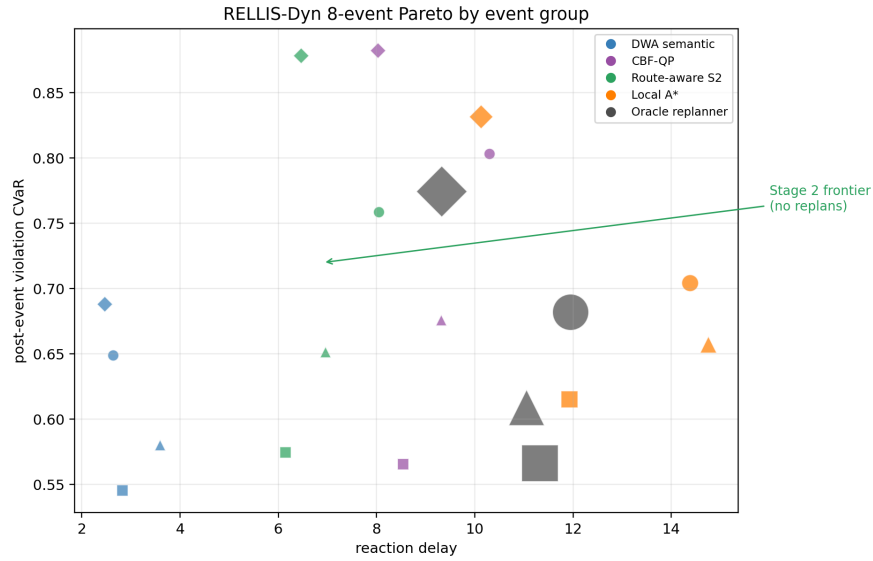


Figure 9: **RELLIS-Dyn 8-event group Pareto.** Each marker is one method on one event group. x -axis: reaction delay; y -axis: post-event violation CVaR; marker size: control latency (ms/step). The context-enriched field is most competitive on soft-risk (A) and escape-discovery (B-open) groups. Reactive baselines lead on moving-obstacle (C) groups.

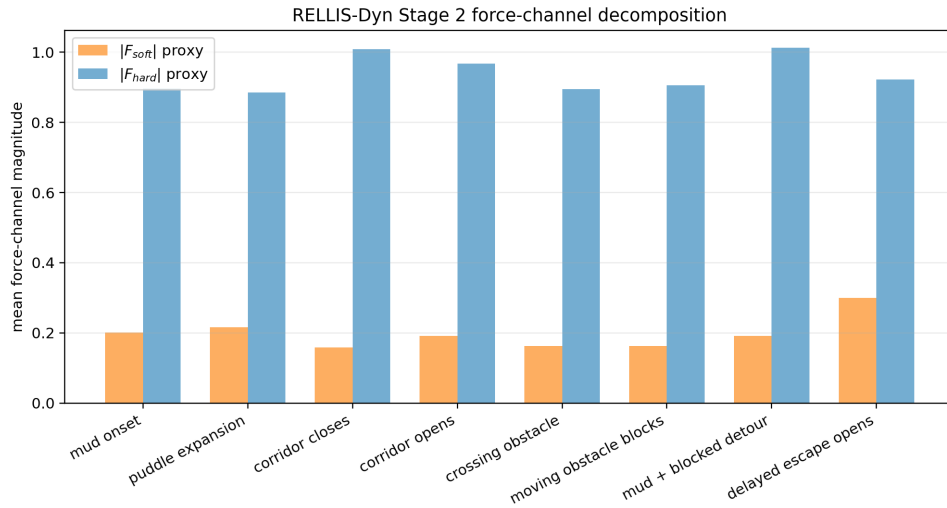


Figure 10: **RELLIS-Dyn force-channel decomposition.** Mean proxy magnitudes of F_{soft} and F_{hard} across eight event types. Soft events activate F_{soft} ; hard-boundary and compound events additionally activate F_{hard} .

Table 18: **Broad highway baseline comparison.** Mean over three scenarios, 200 seeds each. Safety-first rank: collision, off-road, risk, then speed. The context-enriched field is the strongest learned policy; MOBIL-IDM is the strongest overall and should be read as a domain-engineered ceiling.

Method	Family	Rank	Success \uparrow	Coll. \downarrow	Off-rd. \downarrow	Risk \downarrow	Speed \uparrow	Progress \uparrow
MOBIL-IDM	hand-eng.	1/13	1.00	0.00	0.00	5.81	21.29	254.8
Risk-aware MPC	planning	2/13	1.00	0.00	0.00	17.54	13.75	164.0
Chance-const. MPC	planning	3/13	1.00	0.00	0.00	18.34	14.79	176.6
Ours ctx-enriched	learned field	4/13	1.00	0.00	0.00	18.35	18.86	225.8
CBF-QP filter	safety filter	5/13	1.00	0.00	0.00	30.66	14.63	175.2
IDM	hand-eng.	6/13	1.00	0.00	0.00	33.18	14.08	168.6
PPO-Lagrangian	learned const.	7/13	0.75	0.25	0.73	5.01	24.61	105.6
SAC	learned RL	8/13	0.62	0.38	0.38	15.12	22.56	160.7
Ours geometry-only policy	geom.-only	10/13	0.32	0.68	0.32	6.88	23.66	125.9

Table 19: **Highway full scenario-level results.** 200 paired seeds per scenario. The context-enriched field changes behavior when the escape is useful and suppresses it when boxed; see the main-text mechanism ablation (Table 6) for the channel-level explanation.

Scenario	Method	Coll. \downarrow	Off-rd. \downarrow	Success \uparrow	Speed \uparrow	Progress \uparrow	Lane changes
Default	Geometry-only policy	0.05	0.95	0.95	23.56	142.95	0.95
	Ctx-enriched	0.00	0.00	1.00	22.66	271.78	0.00
Slow leader	Geometry-only policy	1.00	0.00	0.00	23.79	44.54	0.00
	Ctx-enriched	0.00	0.00	1.00	26.21	313.94	1.00
Slow leader boxed	Geometry-only policy	0.00	1.00	1.00	13.25	74.48	1.00
	Ctx-enriched	0.00	0.00	1.00	7.57	90.19	0.00

Highway-env: separate trajectory panels with traffic context

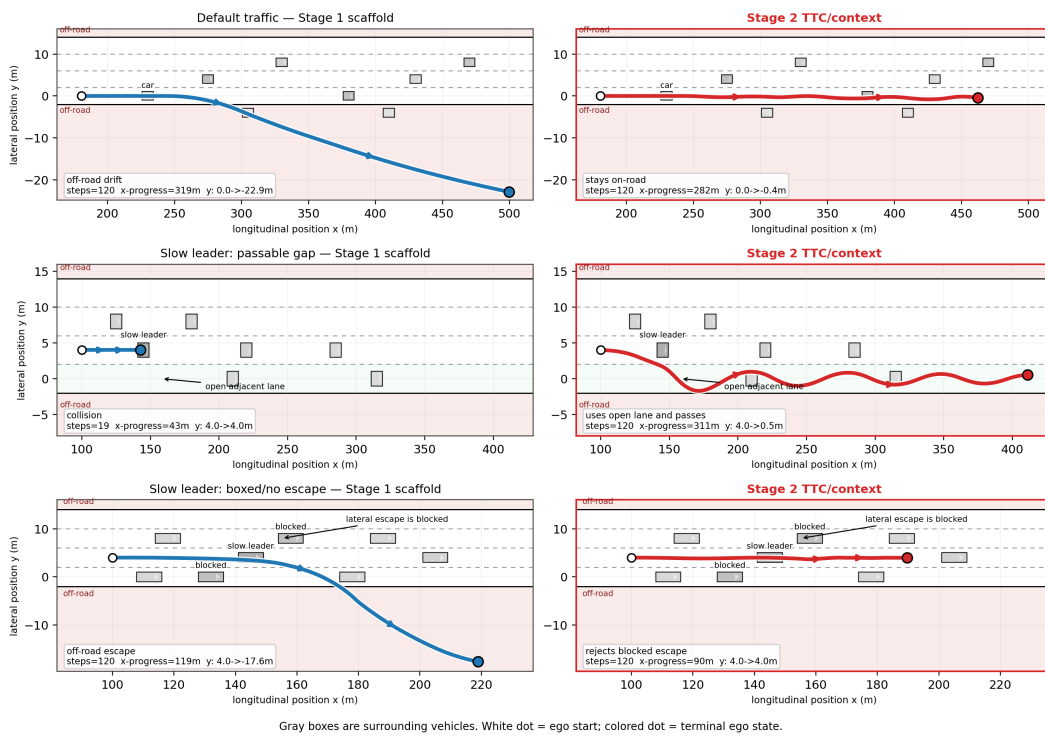


Figure 11: **Highway trajectory panels.** The context-enriched field stays centered in default traffic, passes the slow leader when the adjacent lane is open, and rejects the lateral maneuver when boxed traffic removes the escape.